

# Symmetry and optical selection rules in graphene quantum dots

Rico Pohle,<sup>1</sup> Eleftheria G. Kavousanaki,<sup>2,3</sup> Keshav M. Dani,<sup>2</sup> and Nic Shannon<sup>1</sup>

<sup>1</sup>*Theory of Quantum Matter Unit, Okinawa Institute of Science and Technology Graduate University, Onna-son, Okinawa 904-0495, Japan*

<sup>2</sup>*Femtosecond Spectroscopy Unit, Okinawa Institute of Science and Technology Graduate University, Onna-son, Okinawa 904-0495, Japan*

<sup>3</sup>*Crete Center for Quantum Complexity and Nanotechnology, Department of Physics, University of Crete, 71003, Heraklion, Greece*

(Dated: October 7, 2016)

Graphene quantum dots (GQD's) have optical properties which are very different from those of an extended graphene sheet. In this article we explore how the size, shape and edges of a GQD affect its optical conductivity. Using representation theory, we derive optical selection rules for regular-shaped dots. We find that GQD's whose point-group operations do not commute — for example dots of a rectangular shape — can be distinguished using polarized light. We also carry out explicit calculations of the optical conductivity of GQD's described by a simple tight-binding model, and use these to examine how zigzag and armchair edges impact on their optical properties. For dots of intermediate size ( $> 10\text{nm}$ ) we find that an absorption peak in the low-frequency range of the spectrum makes it possible to distinguish between zigzag and armchair edges. We also clarify the one-dimensional nature of states at the Van Hove singularity in GQD's and graphene, providing a possible explanation for very high exciton-binding energies. Finally we discuss the role of atomic vacancies and shape asymmetry.

## I. INTRODUCTION

Graphene, a single sheet of carbon atoms arranged in a honeycomb lattice, became experimentally accessible in 2004, through perhaps the most innovative use of scotch tape in the 21st century<sup>1,2</sup>. The first of the many surprises of this “wonder material” was that it could be seen at all, using nothing more than an optical microscope<sup>3</sup>. And in fact, the large, universal, and approximately constant optical response of graphene in the visible spectrum is a signature of one of its other remarkable properties — electrons with a relativistic “Dirac” dispersion<sup>4–10</sup>.

Graphene is also a very good conductor of DC electric current<sup>2,11,12</sup>. However in this case, the conductivity measured in experiment is found to depend on the boundaries of the graphene sheet<sup>13–15</sup>, a fact which highlights the topological character of graphene's electronic states<sup>16,17</sup>. Boundary effects are even more pronounced in the graphene nanostructures referred to as “graphene quantum dots” (GQD's). GQD's have a discrete energy spectrum, and can be viewed as large,  $\text{sp}_2$ -bonded, carbon molecules, with electronic states which depend on the size, shape and symmetry of the dot<sup>18,19</sup>.

The possibility of engineering the energy spectrum of a GQD, and therefore its optical properties, has suggested potential applications in fields ranging from quantum computation to solar energy<sup>20–28</sup>. A range of different fabrication techniques are now available for GQD's<sup>29–36</sup>. However, tailoring the properties of a GQD to a specific application requires the ability to fabricate dots with the desired shape, or to post-select for dots with a given shape after fabrication. In either case, understanding the relationship between the size and shape of the dot, and its optical properties, is paramount.

In this Article, we explore how the size, shape and

edge-geometry of a GQD combine to determine its optical conductivity, paying particular attention to the symmetry of the dot, and the optical selection rules which follow from it. Considering regular GQD's with range of different shapes, we first examine how different point-group symmetries lead to different optical selection rules. In the case of GQD's with a non-abelian point-group symmetry — for example rectangular dots — we find that the optical conductivity  $\sigma(\omega)$  depends explicitly on the polarization of the incident light. This result is confirmed by explicit, numerical, calculations of the optical conductivity of regular GQD's, within a simple tight-binding model.

The same numerical approach is used to explore how the optical properties of a GQD evolve into those of a graphene sheet, as the size of the dot is increased. Here we find that edge-geometry plays an important role, with zigzag edges contributing a strong, additional, feature to the optical conductivity within the visible spectrum, for GQD's as large as  $\sim 100\text{nm}$ . This feature is not observable in the thermodynamic limit, and is absent in GQD's with armchair edges, allowing a direct distinction between dots with different edge-types.

We also examine how the strong peak in the optical conductivity of graphene in the ultraviolet evolves out of the spectrum of a GQD. Within a tight-binding model, this peak occurs at twice the energy of the hopping integral, and is associated with a van-Hove singularity in the single-particle density of states. A very similar feature is observed in the optical conductivity of GQD's, where it can be traced to a highly-degenerate set of electronic states with one-dimensional character. The one-dimensional nature of these states suggest a possible explanation for the high binding—energies of excitons in graphene<sup>37–41</sup>.

Finally, we investigate the optical properties of GQD's with irregular shape and disorder, in the form of vacancies in the lattice. In this case, we find a polarization-dependent optical conductivity which polarization depends on the details of each individual, asymmetric dot. We also find new optical features arising from vacancies in the lattice. Averaging over an ensemble of dots restores the polarization-independence of bulk graphene, but does not eliminate new features coming from vacancies.

While graphene is a new phenomenon, the study of the optical properties of two-dimensional (2D) materials has a long history. Theoretical studies of the optical conductivity in 2D systems date back roughly 70 years in the context of single graphite layers<sup>42</sup>, zero-gap semiconductors<sup>43</sup> and d-wave superconductors<sup>44</sup>. Nevertheless, studies explicitly in graphene experienced a sharp increase after its experimental realisation<sup>16,17,45,46</sup>. The existence of Dirac cones in the dispersion relation classifies graphene as a semimetal with novel features like the presence of massless Dirac fermions<sup>2</sup>, an absence of backscattering through electrostatic barriers known as the Klein paradox<sup>47</sup> and an unconventional integer quantum Hall effect<sup>2,48,49</sup>, to name just a few.

The transport and optical properties of graphene have also attracted considerable interest. An important prediction, which predates the discovery of graphene, is that its DC conductivity without disorder takes on the value of<sup>4,50,51</sup>

$$\sigma_{theo}^{DC} = \frac{4}{\pi} \frac{e^2}{h}. \quad (1)$$

Early experiments reported values, which were larger than this prediction by a factor of  $\pi$ , a fact which became known as the ‘‘mystery of a missing pi’’<sup>2,11</sup>. Later studies explained in theory<sup>13–15</sup>, and confirmed in experiment<sup>12</sup>, that the value of  $\sigma^{DC}$  strongly depends on the boundary conditions of the graphene sheet, highlighting the important role of the topology in graphene's electronic states.

Perhaps the most striking feature of graphene's optical conductivity is its universal value

$$\sigma_0 = \frac{\pi}{2} \frac{e^2}{h} \quad (2)$$

over a wide range of frequencies<sup>4,6–10</sup>. This universal optical conductivity is observed in experiments<sup>3,39,52–54</sup>, and falls within the visible spectrum, making it possible to see a single layer of carbon atoms using only an optical microscope<sup>3</sup>. However, theoretical studies showed that disorder can lift this universal value, resulting in an additional peak within this plateau<sup>9</sup>.

The other striking feature of the optical conductivity of graphene is a strong, asymmetric peak at energies  $\sim 4.7$  eV<sup>55</sup>, with a Fano resonance-like line-shape<sup>40</sup>. This peak is seen in electron loss spectroscopy<sup>55</sup> and spectroscopic ellipsometry<sup>38</sup> as well as in optical absorption<sup>38</sup>, transmission<sup>40</sup> and reflection<sup>39,56</sup>. A similar peak is seen in calculations based on a non-interacting tight-binding

model, which can be attributed to a van-Hove singularity in the density of states (DOS)<sup>8</sup>. Once electron-electron interactions are taken into account, this peak is redshifted by  $\Delta = 400 - 600$  meV, which is attributed to an excitonic state strongly coupled to a band continuum<sup>37–41,57</sup>.

The optical properties of graphene change dramatically, once its electrons are confined within a nanostructure. Recently, there has been growing interest in the properties of nanoscale flakes of graphene, commonly referred to as graphene quantum dots (GQD's), graphene nanoislands<sup>33</sup>, or nanographene<sup>58</sup>. This research has also been motivated by potential applications in quantum computing<sup>59</sup>, bioimaging<sup>20–23</sup>, LEDs light converters<sup>24,25</sup>, photodetectors<sup>26,27</sup>, and organic solar cells<sup>28</sup>. GQDs can be synthesized in several ways, e.g. via fragmentation of C<sub>60</sub> molecules<sup>30</sup>, nanoscale cutting of graphite combined with exfoliation<sup>32</sup>, chamber pressure chemical vapor deposition (CP-CVD)<sup>34</sup> and controlled decomposition of hydrocarbons<sup>33</sup>. Furthermore, scanning tunneling microscopy (STM) measurements confirmed the confinement of electronic states in GQD's<sup>19,60–63</sup> and motivated further theoretical studies.

Much like graphene nanoribbons<sup>45</sup>, graphene quantum dots exhibit metallic or insulating behavior depending on the type of their edges, namely zigzag or armchair<sup>64</sup>. GQD's with triangular geometry and zigzag edges show zero energy edge states<sup>65,66</sup>, leading to magnetic effects as edge-state magnetization<sup>67–69</sup> and spin blockade<sup>70</sup>. Studies of optical properties of GQDs have shown signatures of edge states<sup>58</sup>, excitonic effects on the optical absorption spectrum<sup>71,72</sup> and edge-dependent selection rules in triangular dots<sup>73</sup>.

Despite the huge advances made in manufacturing GQD's, there are still obstacles to overcome towards a complete control of size, geometry and edge type. It is in this context that we revisit the question of how size, shape and edge-geometry affect the optical properties of GQD's, paying particular attention to the symmetry of the dots. We do not take interactions between electrons into account, but instead, concentrate on symmetry-controlled properties, which are model independent. In the interest of being able to compare with predictions obtained in the thermodynamic limit, we also calculate the optical conductivity within a tight-binding model known to give a good description of bulk graphene<sup>45</sup>. This makes it possible to explore a large range of dot sizes, at the expense of neglecting correlation effects which may be significant in small GQD's. The remainder of this Article is structured as follows:

In Section II we introduce the tight-binding model used to describe GQD's, and the formalism needed to calculate the polarization-dependent optical conductivity  $\sigma_{\alpha\beta}(\omega)$ , within linear-response theory.

In Section III we use representation theory to analyse the optical selection rules found in GQD's with triangular, hexagonal and rectangular shape. We find that GQD's with an abelian point-group symmetry (in this

case, rectangular GQD's) have an optical conductivity  $\sigma_{\alpha\beta}(\omega)$  which depends on the polarization of the light. The optical response of GQD's with a non-abelian point-group, meanwhile, is independent of polarization.

In Section IV we explore the way in which the optical properties of a GQD with a given shape and edge structure evolve into those of an infinite graphene sheet. We find that qualitative differences persist between GQD's with zigzag and armchair edges, even for dots with linear-dimension  $> 10\text{nm}$ . This suggests that optical measurements may prove a useful way to distinguish GQD's of different edge-types.

In Section V we identify one-dimensional wave functions at energies of the van-Hove singularity of graphene. This reduced dimensionality provides a possible explanation for the unusually high binding-energies of excitons, seen in experiments of graphene<sup>37–41</sup>.

In Section VI we discuss irregular GQD's and present how vacancies and asymmetry affect their optical conductivity. While sample averaging over many randomly shaped asymmetric dots weakens edge-effects and recovers the optical conductivity of graphene, vacancies in the bulk cause additional features similar to those seen in GQD's with zigzag edges.

We conclude in Section VII with a summary of our results.

## II. OPTICAL CONDUCTIVITY CONSISTENT WITHIN TIGHT-BINDING MODEL

### A. Hamiltonian

Many of the electronic properties of graphene can be understood with the tight-binding model on the honeycomb lattice<sup>17,42,45</sup>:

$$\hat{\mathcal{H}}_0 = -t \sum_{\langle ij \rangle, s} (\hat{a}_{i,s}^\dagger \hat{b}_{j,s} + \hat{b}_{j,s}^\dagger \hat{a}_{i,s}), \quad (3)$$

where the sum runs over all nearest-neighbour sites  $i, j$ , using  $t$  as the hopping parameter. The operators  $\hat{a}_{i,s}^\dagger$  ( $\hat{b}_{j,s}^\dagger$ ) and  $\hat{a}_{i,s}$  ( $\hat{b}_{j,s}$ ) respectively create and annihilate electrons with spin  $s = \uparrow, \downarrow$  at site  $i$  ( $j$ ) of sub-lattice  $a$  ( $b$ ). To describe a finite-sized system such as a GQD (Fig. 1), we assume zero hopping beyond the edges of the dot (open boundaries), which in real systems may be realized by passivating the dangling bonds with hydrogen atoms.

Since optical selection rules are intimately related to the symmetries of the dot, it is convenient to consider eigenstates of  $\hat{\mathcal{H}}_0$

$$\hat{\mathcal{H}}_0 |\psi_{n,s}\rangle = E_n |\psi_{n,s}\rangle, \quad (4)$$

in a basis chosen to diagonalise a given symmetry operation,  $\hat{\mathcal{M}}$ , i.e.

$$\hat{\mathcal{M}} |\psi_{n,s}\rangle = \mu_n |\psi_{n,s}\rangle. \quad (5)$$

These eigenstates can in turn be written

$$|\psi_{n,s}\rangle = \sum_i c_{i,n,s} |\phi_{i,s}\rangle, \quad (6)$$

where the coefficients

$$c_{i,n,s} = \langle \psi_{n,s} | \phi_{i,s} \rangle, \quad (7)$$

can be expressed in terms of the local atomic states through

$$\langle \vec{r} | \phi_{i,s} \rangle = \phi_{i,s}(\vec{r}) = w(\vec{r} - \vec{R}_i) \chi_s, \quad (8)$$

where  $w(\vec{r} - \vec{R}_i)$  is a Wannier orbital and

$$\chi_\uparrow = \begin{pmatrix} 1 \\ 0 \end{pmatrix}, \quad \chi_\downarrow = \begin{pmatrix} 0 \\ 1 \end{pmatrix} \quad (9)$$

is a spinor representing the spin degree of freedom. For any given dot, and symmetry operation  $\hat{\mathcal{M}}$ , the energy eigenvalues  $E_n$ , and the corresponding coefficients  $c_{i,n,s}$ , can be found numerically. Since eigenvalues are independent of spin, in much of what follows we can simplify the notation by dropping the index  $s$ .

A useful measure of the properties of the dot is the density of states (DOS)

$$g(\epsilon) = \lim_{\gamma \rightarrow 0} \frac{\gamma}{\pi} \sum_{n=1}^N \frac{1}{(\epsilon - E_n)^2 + \gamma^2} = \sum_{n=1}^N \delta(\epsilon - E_n), \quad (10)$$

where  $N$  stands for the total number of electrons in the system, which is in the case for graphene equal to the total number of sites. For purposes of plotting the DOS, it is convenient to work with a finite value of  $\gamma$  in Eq. (10), which is equivalent to convoluting the DOS with a normalised Lorentzian, of full-width half-maximum  $2\gamma$ .

### B. Optical Conductivity

Our chief measure of the optical properties of a GQD will be its optical conductivity  $\sigma_{\alpha\beta}(\vec{q}, \omega)$ , defined through

$$J_\alpha(\vec{q}, \omega) = \sum_\beta \sigma_{\alpha\beta}(\vec{q}, \omega) E_\beta(\vec{q}, \omega), \quad (11)$$

where  $J_\alpha(\vec{q}, \omega)$  is the current which flows as a result of an applied electric field  $E_\beta(\vec{q}, \omega)$ , and  $\alpha, \beta = x, y, z$ . In what follows we set  $\vec{q} = 0$ , since the wavelength of light at the relevant frequencies is much larger than the size of the dots we consider.

We calculate the optical conductivity within linear-response theory, through the Kubo-formula<sup>74</sup>

$$\sigma_{\alpha\beta}(\omega) = \frac{1}{\omega A} \int_0^\infty dt e^{i\omega t} \langle \psi_0 | [\hat{j}_\alpha^\dagger(t), \hat{j}_\beta(0)] | \psi_0 \rangle + i \frac{n_0 e^2}{m\omega} \delta_{\alpha\beta}, \quad (12)$$

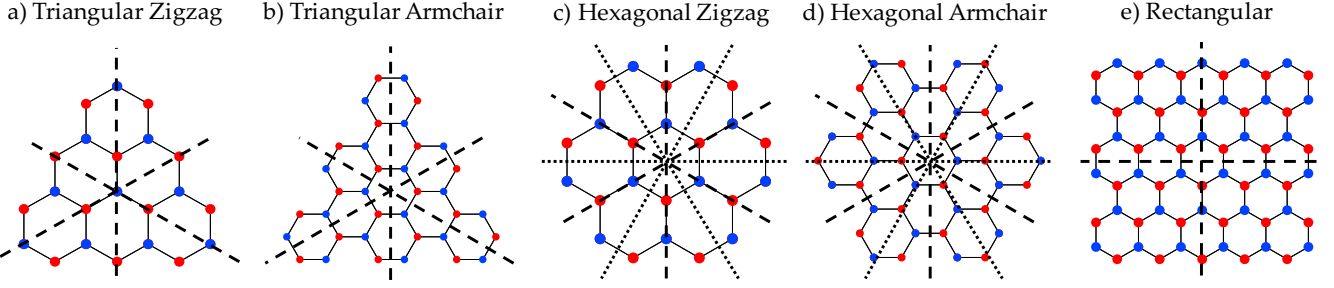


FIG. 1. Regular-shaped Graphene Quantum Dots (GQD's) considered in this Article. (a) Triangular zigzag, (b) triangular armchair, (c) hexagonal zigzag, (d) hexagonal armchair, and (e) rectangular. Triangular and hexagonal dots have symmetries described by the non-abelian point groups  $D_3$  and  $D_6$ , respectively, while rectangular dots have an abelian point group  $D_2$ . Dotted lines represent in-plane mirror axes, while the rotation axis (not shown) is located at the centre of each dot, perpendicular to the plane of the dot.

where  $|\psi_0\rangle$  is the many-body ground state of the tight-binding Hamiltonian  $\mathcal{H}_0$  [Eq. (3)],  $\omega$  the frequency of the externally applied electric field,  $\hat{j}_\alpha$  the current-operator in direction  $\alpha$ ,  $n_0$  the particle density,  $e$  the electron charge,  $m$  the mass of an electron, and  $A$  the area of the dot.

Since electrical charge is a conserved quantity, the appropriate form of the current operator  $\hat{j}_\alpha$  is dictated by the structure of the tight-binding Hamiltonian [Eq. (3)], and is given by<sup>75,76</sup>

$$\hat{j}_\alpha = -it \left( \frac{e}{\hbar} \right) \sum_{ij,s} (R_{i,\alpha} - R_{j,\alpha}) (\hat{a}_{i,s}^\dagger \hat{b}_{j,s} - \hat{b}_{j,s}^\dagger \hat{a}_{i,s}), \quad (13)$$

where  $R_{i,\alpha}$  the  $\alpha$ -component of the position vector of lattice site  $i$ . We note that an inconsistent choice of current operator can lead to incorrect values of the optical conductivity, including deviation from the universal value Eq. (2).

For purposes of calculation, we will use Eq. (7) to express the current operator  $\hat{j}_\alpha$  in terms of the basis  $|\phi_{i,s}\rangle$

$$j_{nm,\alpha} = -it \left( \frac{e}{\hbar} \right) \sum_{ij} c_{ni}^* c_{mj} (R_{i,\alpha} - R_{j,\alpha}), \quad (14)$$

$$\text{Re}[\sigma_\alpha(\omega)] = \lim_{\gamma \rightarrow 0} \frac{2\gamma}{3\sqrt{3}a^2} \frac{t^2}{\hbar\omega} \left( \frac{e^2}{\hbar} \right) \frac{1}{N} \sum_k \frac{|(\vec{\mu}_k)_\alpha \nu_k^* + (\vec{\mu}_k^*)_ \alpha \nu_k|^2}{|\nu_k|^2} \left[ \frac{1}{(\hbar\omega - 2t|\nu_k|)^2 + \gamma^2} - \frac{1}{(\hbar\omega + 2t|\nu_k|)^2 + \gamma^2} \right], \quad (18)$$

where the  $\sum_k$  runs over all  $k$ -values in the Brillouin zone,

$$\nu_k = \sum_{j=1}^3 e^{i\vec{k}\vec{\delta}_j}, \quad \vec{\mu}_k = \sum_{j=1}^3 \vec{\delta}_j e^{i\vec{k}\vec{\delta}_j}, \quad (19)$$

where, for brevity, we drop spin indices and write

$$c_{in} = c_{in,s}. \quad (15)$$

It follows that the real part of the optical conductivity is given by

$$\text{Re}[\sigma_\alpha(\omega)] = \lim_{\gamma \rightarrow 0} \frac{2\gamma\hbar}{A} \frac{1}{\hbar\omega} \sum_{nm} |j_{mn,\alpha}|^2 \frac{f(E_m) - f(E_n)}{(\hbar\omega - E_{nm})^2 + \gamma^2}, \quad (16)$$

where  $E_{nm} = E_n - E_m$  and  $f(E_n)$  is the Fermi function, that describes the particle occupation at energy  $E_n$ . Since, in the absence of magnetic field, current flows parallel to the applied electric field, it is sufficient to consider

$$\sigma_\alpha = \sigma_{\alpha\beta} \delta_{\alpha\beta}. \quad (17)$$

All of the numerical results for  $\sigma(\omega)$  presented in this Article are obtained in the limit of zero-temperature,  $T = 0$ , and calculated for a small but finite value of  $\gamma$ , mimicking the finite lifetime of electronic states.

For many purposes, it is interesting to compare the optical response of a GQD with that of an infinite graphene sheet. We can evaluate this by imposing periodic boundary conditions on the lattice, and taking the thermodynamic limit  $N \rightarrow \infty$ . For  $T = 0$ , in the limit  $q \rightarrow 0$ , transitions are only allowed between states with the same crystal momentum and we find, consistent with the literature<sup>10</sup>,

and the lattice vectors  $\vec{\delta}_j$  are given

$$\vec{\delta}_1 = \frac{a}{2} \{-\sqrt{3}, -1\}, \quad \vec{\delta}_2 = \frac{a}{2} \{\sqrt{3}, -1\}, \quad \vec{\delta}_3 = a \{0, 1\},$$

where  $a$  is the lattice constant.

### III. THE ROLE OF GEOMETRY

Graphene quantum dots with regular shapes can be considered as macroscopic molecules, classified by their point-group symmetry. And, as with conventional molecules, different point groups lead to different optical selection rules, and therefore to different optical properties. In this Article, we consider GQD's of the type shown in Fig. 1, because of their experimental availability and prominence in the existing literature<sup>30,32–34,61</sup>.

The GQD's shown in Fig. 1 can be divided into two groups. Dots (a)–(d) have a non-abelian point group symmetry. Meanwhile the rectangular dot, (e), has an abelian point-group symmetry. We find that, in the non-abelian case, the optical conductivity is *independent* of the polarization of the incident light. On the other hand, in the abelian case, the optical conductivity is polarization-dependent. In what follows, we show explicitly how this result follows for GQD's with triangular ( $D_3$ ) and rectangular ( $D_2$ ) symmetry. The case of hexagonal dots ( $D_6$ ) is discussed Appendix A.

#### A. Optical selection rules for triangular dots

$D_3$	$E$	$2C_3$	$3C_2$
$A_1$	1	1	1
$A_2$	1	1	-1
$E$	2	-1	0

TABLE I. Character Table of the point-group  $D_3$ , describing the symmetry of triangular graphene quantum dots (GQD's) of the type shown in Fig. 1(a) and Fig. 1(b). Eigenstates of a triangular GQD transform with irreducible representations (irreps)  $A_1$ ,  $A_2$  and  $E$ . The corresponding symmetry operations  $E$ ,  $C_3$  and  $C_2$  are defined in Section III A.

GQD's with triangular geometry transform with dihedral point group  $D_3$ . This is the non-abelian group of the lowest order, containing only symmetry operations which do not commute. As shown in the character table (Table I),  $D_3$  comprises the following symmetry elements: identity ( $E$ ),  $2 \times \frac{2\pi}{3}$  rotations in the principle axis ( $2C_3$ ) and 3 reflections on symmetry axes ( $3C_2$ ). Its irreducible representations include the non-degenerate  $A_1$ ,  $A_2$ , and a doubly degenerate  $E$ . The entire group  $D_3$  can be generated from a single mirror and a single rotation operation. We discuss the consequences of each of these two symmetry operations in turn, below.

##### 1. Linearly polarized light: selection rules from mirror symmetry

When considering linearly-polarized light, making use of the mirror symmetry is a natural choice (Fig. 1(a)).

We describe a reflection by the operator  $\hat{\mathcal{M}}_y$ , which mirrors the dot along the  $y$ -axis, and diagonalise the Hamiltonian in a basis

$$\hat{\mathcal{M}}_y|\psi_n\rangle = \mu_n|\psi_n\rangle, \quad \mu_n = 1, -1 \quad (20)$$

that respects this mirror symmetry, where, once again, we have dropped the spin-index  $s$  for brevity.

Using the fact that only the  $x$ -component of the current operator switches sign under reflection,

$$\hat{\mathcal{M}}_y^{-1} \hat{j}_x \hat{\mathcal{M}}_y = -\hat{j}_x \quad (21)$$

$$\hat{\mathcal{M}}_y^{-1} \hat{j}_y \hat{\mathcal{M}}_y = \hat{j}_y \quad (22)$$

we find that the matrix elements of the current operator are given by

$$\begin{aligned} \langle\psi_n|\hat{j}^x|\psi_m\rangle &= \langle\psi_n|\hat{\mathcal{M}}_y^{-1} \hat{\mathcal{M}}_y \hat{j}^x \hat{\mathcal{M}}_y^{-1} \hat{\mathcal{M}}_y|\psi_m\rangle \\ &= (-1) \mu_n \mu_m \langle\psi_n|\hat{j}^x|\psi_m\rangle. \end{aligned} \quad (23)$$

This leads to the optical selection rule

$$\mu_n \mu_m = -1, \quad (24)$$

which implies that, for  $x$ -polarized light, only transitions between states of opposite mirror symmetry are allowed. It follows from the character table, Table I, that allowed transitions will be between states transforming with the irreducible representations

$$A_1, E \leftrightarrow A_2, E. \quad (25)$$

In Fig. 2 we show how the optical selection rule Eq. (25) is borne out by explicit calculation of the optical conductivity for the smallest triangular GQD with zigzag edges. The transitions corresponding to the main features in  $\sigma(\omega)$ , labelled I and II in Fig. 2(a), are shown in Fig. 2(b). As anticipated, the matrix elements of the current operator  $|j_{nm,x}|^2$  are non-zero only for transitions between states of different mirror symmetry [cf Fig. 2(d)].

Similarly, in the case of  $y$ -polarized light, where the current operator is symmetric under reflection [Eq. (22)], we find the following selection rule:

$$\mu_n \mu_m = 1. \quad (26)$$

In this case, only transitions between states of the same symmetry are allowed, and it follows that

$$A_1, E \leftrightarrow A_1, E; \quad A_2, E \leftrightarrow A_2, E. \quad (27)$$

Once again this result is confirmed by explicit calculations, as shown in Fig. 2(c) and Fig. 2(e).

Since the selection rules for  $x$ - and  $y$ -polarization, Eq. (25) and Eq. (27), are different, it might seem reasonable to expect that the optical conductivity would also be polarization-dependent. However, as can be seen from the numerical results in Fig. 2(a), this is not the case — the optical conductivity of a triangular GQD is independent of polarization. To understand why this is true, we need also to consider the consequences of rotational symmetry.



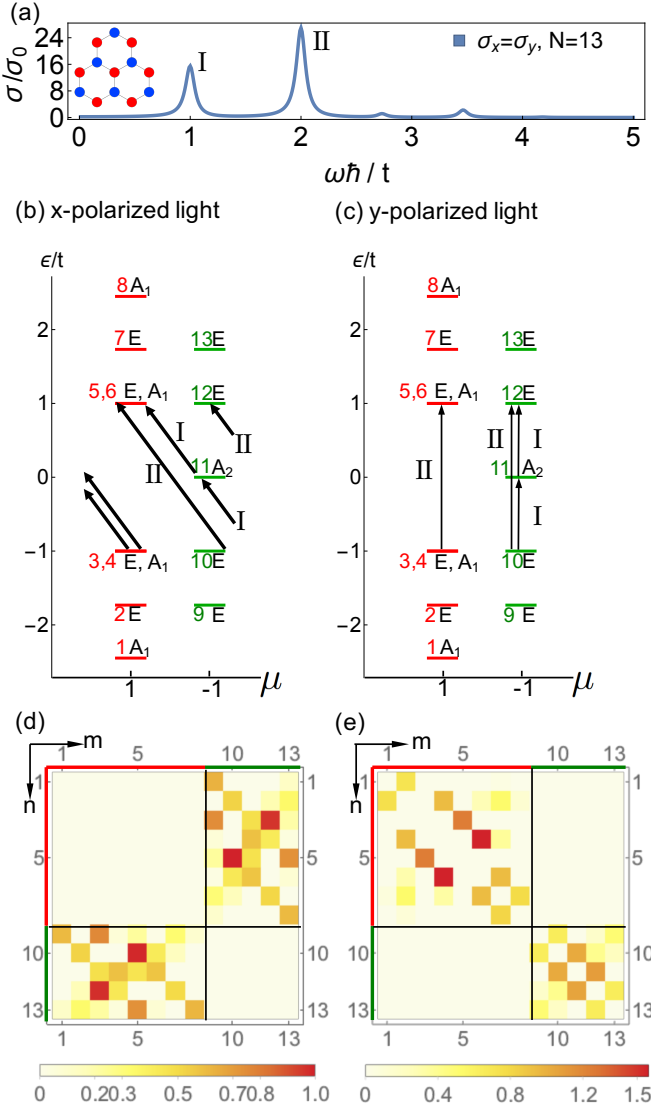


FIG. 2. Optical selection rules for a triangular graphene quantum dot (GQD), in linearly-polarized light. (a) Optical conductivity  $\sigma(\omega)$ , showing equivalence of results for  $x$ - and  $y$ - polarized light. (b) and (c) Spectrum of the corresponding tight-binding model Eq. (3), in the mirror basis Eq. (20), showing the different allowed transitions for  $x$ - and  $y$ -polarized light. (d) and (e) Matrix elements of the corresponding current operators  $|j_{nm,x}|^2$  and  $|j_{nm,y}|^2$  [cf. Eq. (14)]. Results for  $\sigma(\omega)$  were calculated from Eq. (16), setting  $\gamma/t = 0.05$ , for the smallest triangular GQD with zigzag edges ( $N = 13$ ). Eigenstates are labelled according to their quantum number  $n = 1 \dots 13$ , eigenvalue  $\mu_n = \pm 1$  [Eq. (20)] and corresponding irrep [cf. Table I].

## 2. Circularly-polarized light: selection rules from rotational symmetry

In the case of circularly-polarized light, it is natural to think about the rotational symmetry of the dot. In analogy with the previous discussion, we describe a rotation

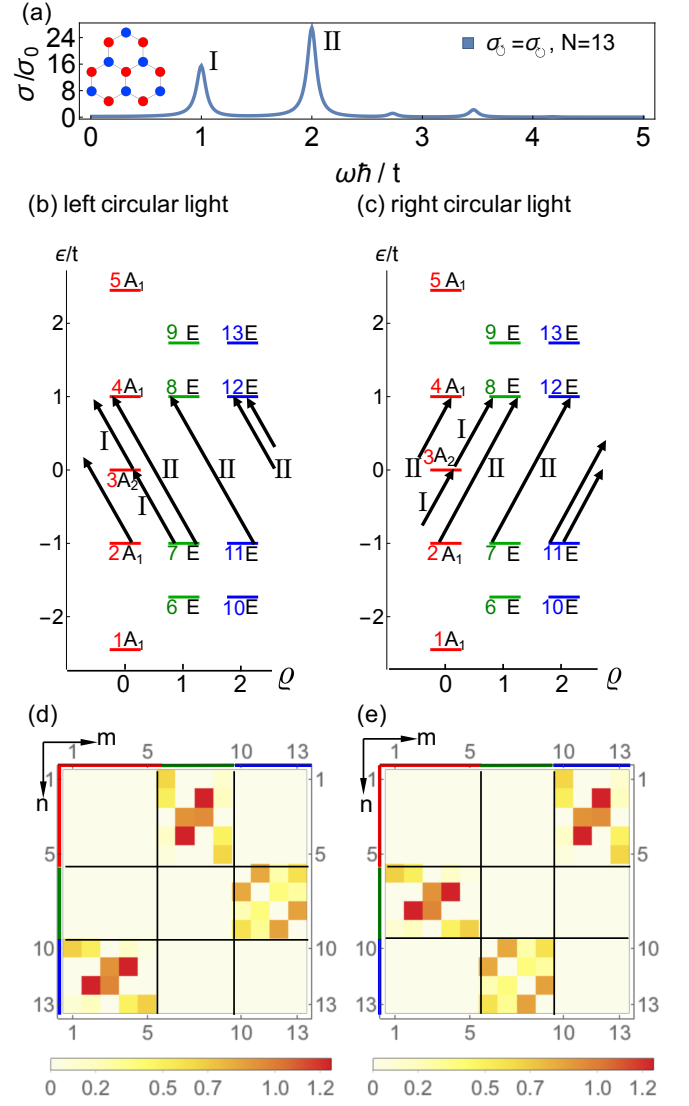


FIG. 3. Optical selection rules for a triangular graphene quantum dot (GQD), in circularly-polarized light. (a) Optical conductivity  $\sigma(\omega)$ , showing equivalence of results for left- and right- circularly polarized light. (b) and (c) Spectrum of the corresponding tight-binding model Eq. (3), in the rotation basis Eq. (28), showing the different allowed transitions for left- and right- circularly polarized light. (d) and (e) Matrix elements of the corresponding current operators  $|j_{nm,\odot}|^2$  and  $|j_{nm,\ominus}|^2$  [cf. Eq. (14)]. Results for  $\sigma(\omega)$  were calculated from Eq. (16), setting  $\gamma/t = 0.05$ , for the smallest triangular GQD with zigzag edges ( $N = 13$ ). Eigenstates are labelled according to their quantum number  $n = 1 \dots 13$ , eigenvalue  $\mu_n = e^{i\frac{2\pi}{3}\rho_n}$ ,  $\rho_n = 0, 1, 2$  [Eq. (29)] and corresponding irrep [cf. Table I].

of  $\frac{2\pi}{3}$  around the principal axis by the operator  $\hat{\mathcal{R}}_{2\pi/3}$ . The eigenstates of the Hamiltonian are now written in a basis that respects the rotational symmetry of the dot, i.e.

$$\hat{\mathcal{R}}_{2\pi/3}|\psi_n\rangle = \mu_n|\psi_n\rangle, \quad (28)$$

where

$$\mu_n = e^{i\frac{2\pi}{3}\rho_n}, \rho_n = 0, 1, 2. \quad (29)$$

In analogy with Eq. (23), we can calculate the matrix elements of the current operator for currents flowing circularly to the left ( $j_\odot = j_x + ij_y$ ) and to the right ( $j_\odot = j_x - ij_y$ ). We obtain the following optical selection rule

$$e^{i\frac{2\pi}{3}(\ell_n - \ell_m + 1)} = 1, \quad (30)$$

for left-circularly polarized light, and

$$e^{i\frac{2\pi}{3}(\ell_n - \ell_m - 1)} = 1, \quad (31)$$

for right-circularly polarized light.

It follows from Eq. (30) that the allowed transitions for left-circularly polarized light are anti-cyclic

$$\rho = 0 \rightarrow 2 \rightarrow 1 \rightarrow 0, \quad (32)$$

while Eq. (31) implies that the allowed transitions for right-circularly polarized light are cyclic

$$\rho = 0 \rightarrow 1 \rightarrow 2 \rightarrow 0. \quad (33)$$

As a consequence, transitions are only possible between states transforming with the irreps

$$A_1, A_2 \leftrightarrow E \quad (34)$$

and, as a consequence, transitions between states transforming with  $A_1$  and  $A_2$  are forbidden. Examples of allowed transitions, and their corresponding matrix elements are shown in Fig. 3.

It is natural to think of these selection rules in terms of the exchange of angular momentum between a photon and the electrons in a GQD. This intuition must be approached with a little caution, as  $\hat{\mathcal{R}}_{2\pi/3}$  generates discrete, and not continuous rotations<sup>77</sup>. However, within this rotation-symmetry basis, we find that states with  $\rho = 1, 2$  have a net circulation of current on their bonds, which is to say a net magnetic moment. All of these states transform with the  $E$ -irrep, and are Kramers doublets — degenerate pairs of states whose current-flow is related by time-reversal symmetry. Applying a magnetic field lifts the degeneracy of these Kramers doublets — a subject explored in more detail in Ref. 78. An example of the current flow within such a Kramers doublet is shown in Fig. 14 in Appendix B.

The selection rules for circularly-polarized light also provide the missing piece of the puzzle as to why the optical conductivity for linearly-polarized light is independent of polarization [cf. Fig. 2, Section III A 1]. At first glance, the selection rules for  $x$ -polarized light, Eq. (25), permit transitions between states transforming with the  $A_1$  and  $A_2$  irreps, while the selection rules for  $y$ -polarized light, Eq. (27), do not. However, it is always possible to decompose circularly-polarized light into linear-polarized components. And the selection rules for circularly polarized light, Eq. (30), and Eq. (31) explicitly

	x	y
$C_2$	$A_1, E \leftrightarrow A_2, E$	$A_1, E \leftrightarrow A_1, E$ $A_2, E \leftrightarrow A_2, E$
$C_3$	$A_1, A_2 \leftrightarrow E$	
total	$A_1, E \leftrightarrow E$ $A_2, E \leftrightarrow E$	$A_1, E \leftrightarrow E$ $A_2, E \leftrightarrow E$

TABLE II. Selection rules for optical transitions in triangular Graphene Quantum Dots (GQD's) of the type shown in Fig. 1 (a) and (b). While individual transitions may be sensitive to polarization, the total response does not distinguish between  $x$ - and  $y$ -polarized light.

forbid transitions between the  $A_1$  and  $A_2$  irreps, since these have the same rotation eigenvalue  $\mu = 1$  ( $\rho = 0$ ). As a consequence, the final “total” selection rules for  $x$ - and  $y$ -polarized light (cf. Table II) are the same

$$A_1, E \leftrightarrow E; \quad A_2, E \leftrightarrow E, \quad (35)$$

and the optical response is independent of the polarization.

This result can be important for experiments with e.g. solutions of GQD's, as the absorption spectra are completely polarization-independent.

## B. Optical selection rules for rectangular dots

$D_2$	$E$	$C_2(z)$	$C_2(y)$	$C_2(x)$
$A$	1	1	1	1
$B_1$	1	1	-1	-1
$B_2$	1	-1	1	-1
$B_3$	1	-1	-1	1

TABLE III. Character Table of the point-group  $D_2$ , describing the symmetry of rectangular graphene quantum dots (GQD's) of the type shown in Fig. 1(e). Eigenstates of a triangular GQD transform with irreducible representations (irreps)  $A$ ,  $B_1$ ,  $B_2$  and  $B_3$ . The corresponding symmetry operations  $E$ ,  $C_2(z)$ ,  $C_2(y)$  and  $C_2(x)$  are defined in Section III B.

In the previous discussion, we explained in detail how the selection rules in GQD's with a non-abelian symmetry result in a polarization-independent optical conductivity. Here we discuss an example of a GQD with abelian symmetry, the rectangular dot of Fig. 1(e), which has the symmetry of the  $D_2$  group. We show that the optical conductivity in this case is polarization dependent.

As seen in Table III, the  $D_2$  group includes the following symmetry elements: identity ( $E$ ), in-plane reflections ( $C_2(x)$  and  $C_2(y)$ ), and one  $\pi$  rotation ( $C_2(z)$ ) around the principle axis. All symmetry operations in this point-group commute with each other and lead to one-dimensional irreducible representations, which include the symmetric  $A$ , and the antisymmetric  $B_1, B_2, B_3$ .

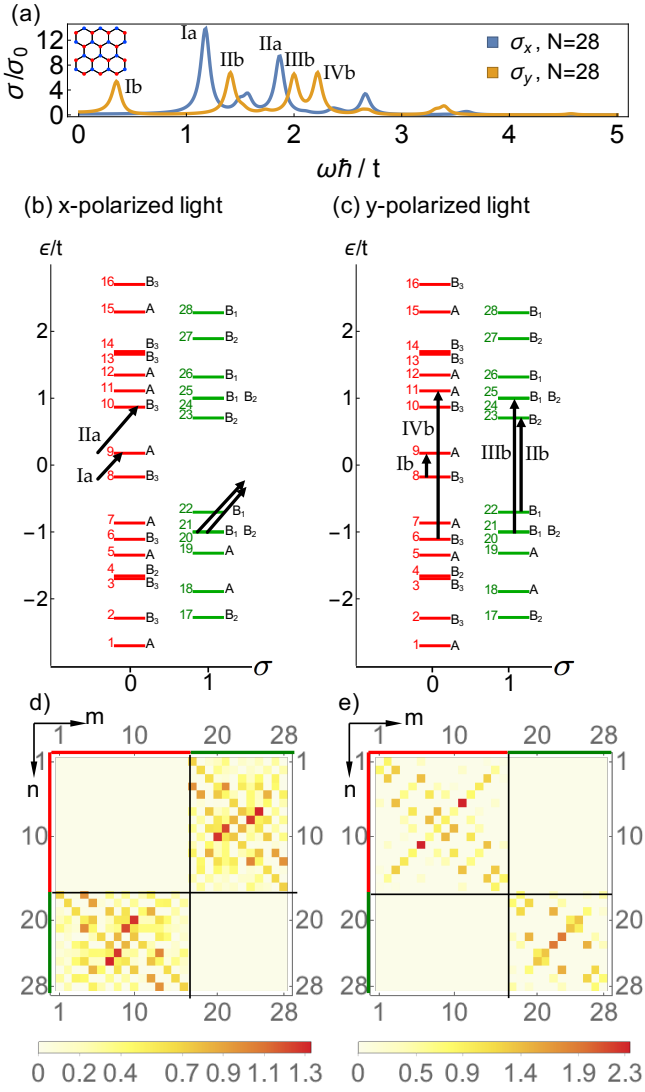


FIG. 4. Optical selection rules for a rectangular graphene quantum dot (GQD), in linearly-polarized light. (a) Optical conductivity  $\sigma(\omega)$ , showing different results for  $x$ - and  $y$ - polarized light. (b) and (c) Spectrum of the corresponding tight-binding model Eq. (3), in the mirror basis Eq. (20), showing the different allowed transitions for  $x$ - and  $y$ -polarized light. (d) and (e) Matrix elements of the corresponding current operators  $|j_{nm,x}|^2$  and  $|j_{nm,y}|^2$  [cf. Eq. (14)]. Results for  $\sigma(\omega)$  were calculated from Eq. (16), setting  $\gamma/t = 0.05$ , for a rectangular GQD of size  $N = 28$ . Eigenstates are labelled according to their quantum number  $n = 1 \dots 28$ , eigenvalue  $\mu = \pm 1$  [Eq. (20)] and corresponding irrep [cf. Table III].

We repeat the same derivation as before to obtain the optical selection rules for  $x$ - and  $y$ - polarized light, by considering the  $C_2(x)$  and  $C_2(z)$  symmetries separately. The results are shown in Table IV. In this case, the allowed transitions are different for  $x$ - and  $y$ -polarization.

This result is confirmed by our numerical calculations, shown in Fig. 4 for the smallest rectangular GQD.

	x	y
$C_2(x)$	$A, B_3 \leftrightarrow B_1, B_2$	$A, B_3 \leftrightarrow A, B_3$ $B_1, B_2 \leftrightarrow B_1, B_2$
$C_2(z)$	$A, B_1 \leftrightarrow B_2, B_3$	
total	$A \leftrightarrow B_2$ $B_3 \leftrightarrow B_1$	$A \leftrightarrow B_3$ $B_1 \leftrightarrow B_2$

TABLE IV. Selection rules for optical transitions in rectangular Graphene Quantum Dots (GQD's) of the type shown in Fig. 1 (e). Unlike in triangular GQD's the total response does distinguish between  $x$ - and  $y$ -polarized light and cause a polarization-dependent optical conductivity as shown in Fig. 4.

The optical conductivity is very different for  $x$ - and  $y$ -polarization (Fig. 4(a)). As an example, the transition from state 8 to 9 is allowed only for  $y$ -polarized light [see Fig. 4(b) and (c)] and creates the peak Ib in  $\sigma_y(\omega)$ , while  $\sigma_x = 0$  at the same energy.

In summary, we have shown that for GQD's with abelian symmetry, the optical selection rules result in a polarization-dependent optical conductivity, in contrast with the case of GQD's with non-abelian symmetry.

#### IV. THE ROLE OF EDGE TYPES

In Section III we have explored the role of symmetry on the optical conductivity, and shown that the polarization of light can be used to distinguish between dots of abelian and non-abelian point-group symmetry.

In this section, we explore the role of edge type in GQD's by studying the optical conductivity  $\sigma(\omega)$  for triangular, hexagonal and rectangular GQD's with zigzag and armchair edges and various sizes. Using exact diagonalization of the Hamiltonian (Eq. 3), we show the size evolution of  $\sigma(\omega)$  for dots with a total number of sites up to  $N \approx 25,000$  ( $\sim 40$  nm) and find features which allow us to separate between dots of zigzag and armchair edges.

Fig. 5 shows an overview of the density of states and optical conductivity for the five different regular-shaped GQD's considered in this Article, for sizes up to  $N \approx 10,000$  sites. Triangular GQD's with zigzag edges [Fig. 5(a)] show a peak in the DOS at zero energy for all dot sizes, due to a large number of states localized on the edge that have exactly  $\epsilon = 0$  within the tight-binding model<sup>65,79</sup>. The number  $N_0$  of these “zero-energy” states increases linearly with dot size:  $N_0 = N_h - 1$ <sup>64</sup> (see Table V), where  $N_h$  is the number of hexagons per side of the GQD. In the thermodynamic limit the number of edge-states is negligible compared to the total number of states ( $N_0/N \rightarrow 0$ ), thus recovering graphene's zero DOS at  $\epsilon = 0$ .

As seen in Fig. 5(c) and (e), the DOS shows also a feature at zero-energy in hexagonal zigzag and rectangular GQD's for sizes  $N \gtrsim 300$ . In fact, for these dots,



		Triangular Zigzag	Triangular Armchair	Hexagonal Zigzag	Hexagonal Armchair	Rectangular
$L$		$\sqrt{3}(N_h + 1)a$	$3N_h a$	$\sqrt{3}(N_h - 1/3)a$	$(3N_h - 2)a$	$L_x = \sqrt{3}(2N_h - 1)a$ $L_y = 2.5N_h a$
$N$		$(N_h + 1)^2 + 2N_h$	$\frac{3}{4}(N_h + 2)N_h$	$6N_h^2$	$9N_h((N_h/2) - 1) + 6$	$2(4N_h^2 - N_h)$
$N_0$		$N_h - 1$	0	0	0	0
$N_t$	$N_h$ even	3	0	3	$3N_h$	$N_h$
	$N_h$ odd	3	$\frac{1}{2}(3N_h + 1)$	$N_h + (-1)^{(N_h+1)/2}$	$4N_h - 3$	$N_h + 1$

TABLE V. Finite-size scaling of degeneracies for different types of regularly-shaped GQD's, within a tight-binding model, Eq. (3).  $L$  is the length of the edge of the GQD,  $a$  is the lattice constant,  $N_h$  the number of hexagons per side of the GQD,  $N$  is the total number of sites,  $N_0$  the number of zero-energy states, and  $N_t$  the number of states at energy  $\epsilon = t$ . For rectangular GQD's  $N_h$  refers to the number of hexagons on the side with the armchair edges.

there are no states with the exact value  $\epsilon = 0$  (Table V). However a finite number of states in the vicinity of zero energy approach zero for large dot sizes, resulting in a distinct peak in the DOS.

On the other hand, for dots without any zigzag edges [Fig. 5(b) and (d)],  $g(\epsilon = 0)$  is zero for all sizes.

Graphene's DOS exhibits two characteristic peaks at  $\epsilon = \pm t$  (van-Hove singularities)<sup>45</sup>. Fig. 5 clearly shows that these peaks are recovered for large dots in all shapes and edge types. They are due to the presence of states with energy exactly  $\epsilon = \pm t$ . For most dots, their number  $N_t$  scales linearly with dot size (see Table V). However, unlike the case for zero-energy states, their contribution to the DOS at  $\pm t$  does not disappear in the thermodynamic limit. States with energies close to  $\pm t$  converge to  $\epsilon = \pm t$  in the thermodynamic limit, causing the Van Hove singularities known in graphene. We have found analytical expressions for the wave functions of states with exactly  $\epsilon = \pm t$  and will discuss them more detailed in Section V.

Transitions between states of  $\epsilon = \pm t$  cause a characteristic peak in the optical conductivity for  $\hbar\omega = 2t$ . The size-evolution shows that the intensity of this peak is shape and edge-type dependent, though particularly pronounced in dots with armchair edges. However, for large enough sizes all GQD's show a asymmetric Fano resonance-like line-shape, similar to the one in graphene<sup>39,40,80</sup>.

Interestingly, all GQD's with at least some zigzag edges, show an additional peak at  $\hbar\omega = t$  at least for sizes larger than  $N > 1000$ , because of transitions between zero-energy states and states at  $\epsilon = \pm t$ . This peak does not appear in the case of dots with purely armchair edges, thus providing a way to differentiate between the two edge types.

Rectangular dots show a different behaviour of the optical conductivity for  $x$ - and  $y$ - polarized light [Fig. 5(e)-(f)], as explained in Sec. III B. When the electric field is in parallel with the zigzag edges ( $x$ -axis for these dots), the additional peak at  $\hbar\omega = t$  shows up. This is due to the fact that the zero-energy states are localised on the zigzag edges, causing a non-zero current. On the other hand, for  $y$ -polarized light the optical conductivity does

not exhibit this feature.

To get further insight in the size evolution of the peak at  $\hbar\omega = t$ , we plot the optical conductivity for dot sizes of  $N \approx 5,000 - 25,000$  ( $\approx 20 - 40$  nm) in Fig. 6 and compare to results to the analytical solution for graphene in its thermodynamic limit (see Eq. 18).

As seen in the right panels of Fig. 6, the optical conductivity for GQD's with armchair edges converges slowly to the graphene limit, uniformly for all energies. On the other hand,  $\sigma(\omega)$  for dots with zigzag edges has a more complicated behaviour (left panels of Fig. 6). The peak at  $\hbar\omega = t$  is well distinguishable from the background for sizes up to  $N \approx 25,000$  ( $\sim 40$  nm). For values lower in frequency than this peak, the difference to the graphene limit is larger than in the case of armchair edges. This can be explained by transitions occurring between states of  $\epsilon < t$  and states of zero-energy, which are absent in armchair dots. For  $\hbar\omega > t$ ,  $\sigma(\omega)$  coincides with the graphene limit.

As seen in Fig. 6, the plateau of the optical conductivity exhibits strong oscillations. However, in the thermodynamic limit, it approaches the universal conductivity of graphene,  $\sigma_0$ . This is seen in Fig. 7(a) where the finite-size scaling of the peak at  $\hbar\omega/t \approx 0.1$  is shown for all dots under consideration. For all GQD's, this peak approaches the universal conductivity  $\sigma_0$  within  $\lesssim 2\%$ .

In Fig. 7(b) we show the finite-size scaling of the peak at  $\hbar\omega/t = 1$  for GQD's with zigzag edges. We find that this peak approaches the value of graphene quadratically due to its inverse system size  $1/N$ .

In summary, we discussed the optical conductivity of GQD's for a variety of shapes, edge types and sizes up to the thermodynamic limit. We showed that polarization along a zigzag edge causes a distinct peak in  $\sigma(\omega)$  at  $\hbar\omega = t$ . This effect may be used as a way to distinguish between GQD's with zigzag and armchair edges.

## V. LOCALIZED STATES WITH ENERGY $\epsilon/t = \pm 1$

As discussed in Sec. IV, all GQD's exhibit states with an exact energy  $\epsilon = \pm t$ . The number of such states

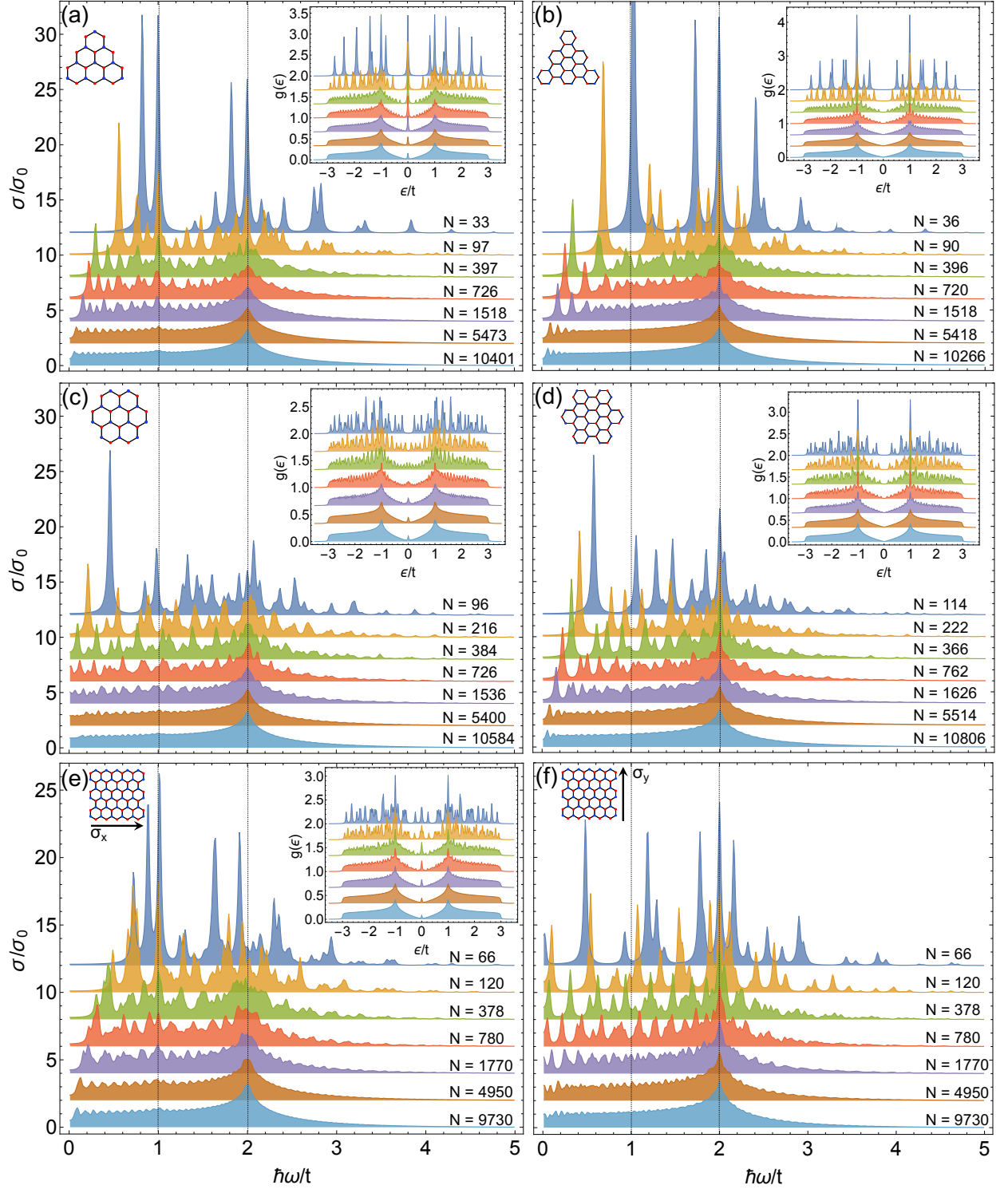


FIG. 5. Evolution of the optical conductivity  $\sigma(\omega)$  and density of states  $g(\epsilon)$  of the regular-shaped graphene quantum dots (GQD's) shown in Fig. 1, as a function of the size of the dot. (a) Triangular zigzag, (b) triangular armchair, (c) hexagonal zigzag, (d) hexagonal armchair, and (e)–(f) rectangular GQD for both  $x$ - and  $y$ -polarized light. We find that states with  $\epsilon = \pm t$  exist in all dots, but are generally more pronounced in dots with armchair edges, causing dominant peaks at  $g(\epsilon = \pm t)$ . For all dots with zigzag edges, there are states in the vicinity of  $\epsilon = 0$ , causing an additional absorption peak at  $\hbar\omega/t = 1$ . All results were calculated within the tight-binding model Eq. (3), and have been convoluted with a Lorentzian of width  $\gamma/t = 0.05$  [cf. Eq. (10), Eq. (16)].

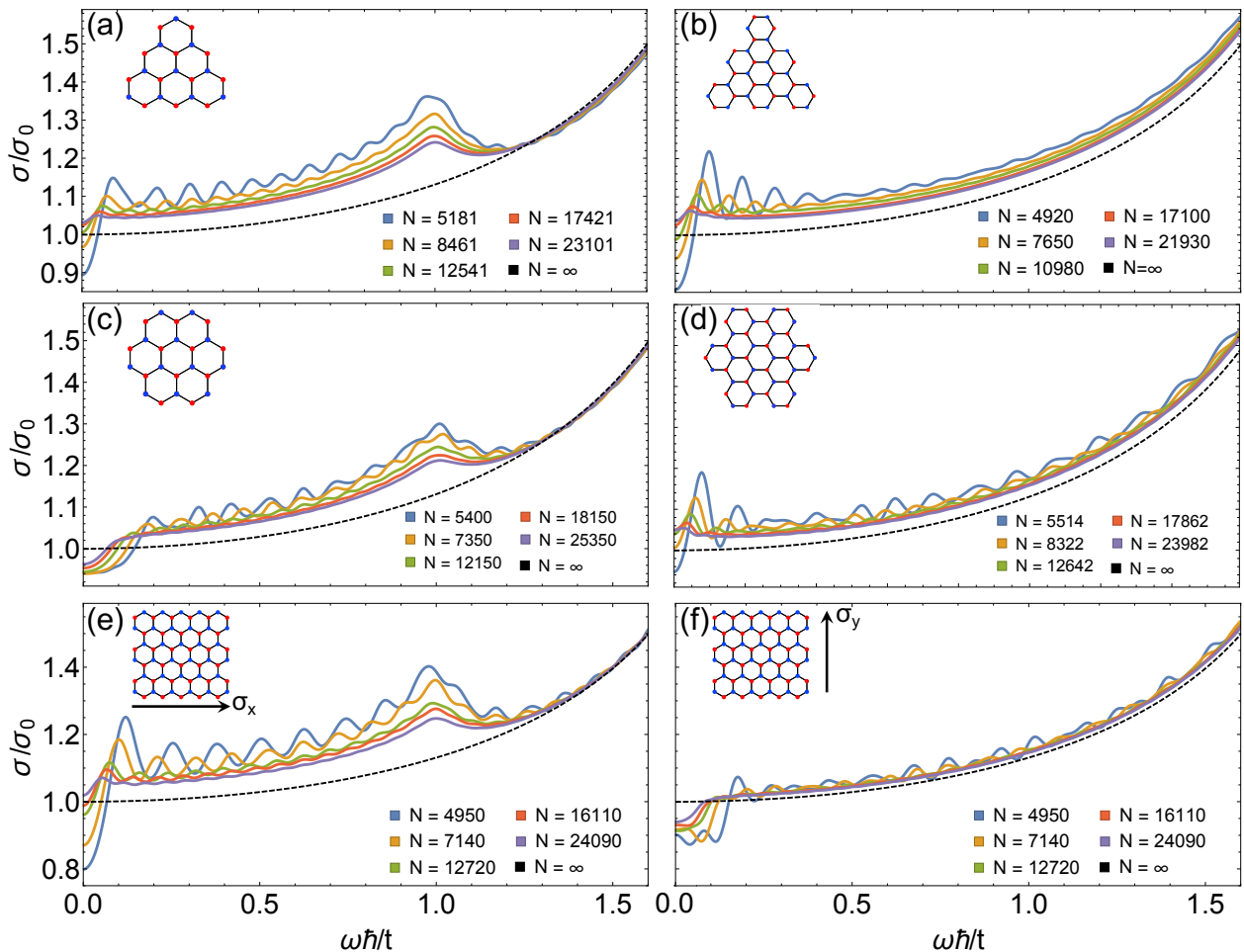


FIG. 6. Low frequency part the optical conductivity  $\sigma(\omega)$  as shown in Fig. 5. (a) Triangular zigzag, (b) triangular armchair, (c) hexagonal zigzag, (d) hexagonal armchair, (e)-(f) rectangular graphene quantum dot (GQD) for both  $x$ - and  $y$ - polarized light, for sizes up to  $N \approx 25,000$ . The peak at  $\hbar\omega/t = 1$  in  $\sigma(\omega)$  for dots with zigzag edges (polarization parallel to the zigzag edge) is distinguishable from the featureless conductivity of dots with armchair edges. We compare the results to the analytical solution for a graphene sheet in its thermodynamic limit (see Eq. (18) – dashed line). All results were calculated within the tight-binding model Eq. (3), and have been convoluted with a Lorentzian of width  $\gamma/t = 0.05$  [cf. Eq. (16)].

depends on the shape and edge type of the GQD and, in most cases, scales linearly with the dot size (Table V). In this section we shed light onto the microscopic nature of these states. We present an analytical solution for their wave functions and show that these states exhibit an one-dimensional (1D) character.

The fact that the energy of these states,  $\epsilon = \pm t$ , coincides with the hopping energy between adjacent sites in the tight-binding Hamiltonian (Eq. 3), motivates us to seek for wavefunctions for which electron hopping takes place on single bonds in the honeycomb lattice. Fig. 8 shows an example of such a wave function for a triangular zigzag GQD with energy  $\epsilon = t$  (anti-binding). The wave function  $|\psi_t\rangle$  is a linear combination of Wannier functions (Eq. 6),

$$|\psi_t\rangle = \sum_i c_{t,i} |\phi_i\rangle, \quad (36)$$

where  $c_{t,i}$  are appropriately chosen to be  $\pm 1$  at the red '+' and blue '-' sites respectively. In the case of Fig. 8(a), the wave function is explicitly written as

$$|\psi_t\rangle \propto -|\phi_3\rangle + |\phi_6\rangle + |\phi_4\rangle - |\phi_7\rangle - |\phi_5\rangle + |\phi_8\rangle \quad (37)$$

which can be directly shown to satisfy  $\hat{H}|\psi_t\rangle = t|\psi_t\rangle$ . Eq. (37) has the energy  $\epsilon = t$  because electron hopping is non-zero only between pairs of atoms, highlighted in Fig. 8(a). Hopping to e.g. site 1 is cancelled out because of the opposite coefficients in sites 3 and 4.

In a similar way, we can construct a binding wave function with  $\epsilon = -t$  as seen in Fig. 8(b).

We note that these wave functions are 1D-like, since they are non-zero only on pairs of sites along a 1D ladder. This is consistent with their 1D scaling behaviour shown in Table V.

The key for the existence of such states is the presence

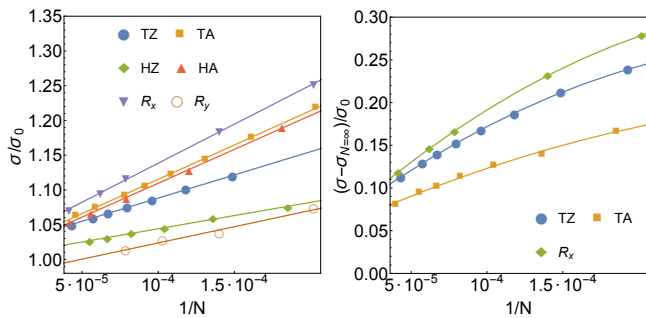


FIG. 7. Finite size scaling of the dominant features in the optical conductivity  $\sigma(\omega)$  from Fig. 6. (a) Linear scaling of the peak maximum for  $\hbar\omega/t < 0.2$ , showing the trend for all graphene quantum dots (GQD's) to reach the universal optical conductivity  $\sigma_0$  in the thermodynamic limit at low frequencies, (b) quadratic scaling of the peak maximum at  $\hbar\omega/t = 1$  (just for GQD's with armchair edges) approaching the value for infinite graphene for large system sizes.

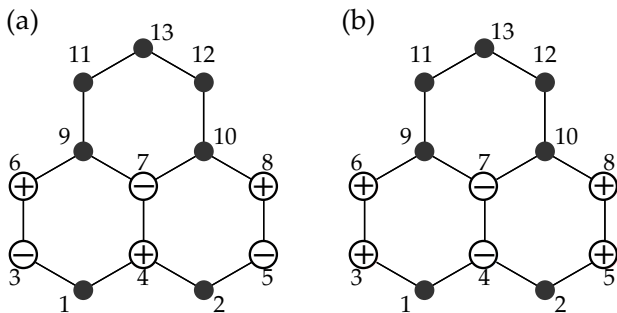


FIG. 8. An example of a 1-dimensional wave function at energy  $\epsilon = \pm t$  in the smallest triangular graphene quantum dot (GQD) with zigzag edges. (a) Anti-binding ( $\epsilon = t$ ) wave function (see Eq. (37)), (b) binding ( $\epsilon = -t$ ) wave function. Plus (minus) denotes the probability amplitude of  $c_{\pm t,i} = +1$  ( $c_{\pm t,i} = -1$ ) of the wave function on site  $i$  (as defined in Eq. (36)). For all other sites we find  $c_{\pm t,i} = 0$ . Such configurations ensure that hopping outside the highlighted sites vanishes.

of a pair of atoms on the edge of the GQD for which each atom has one bond less. This allows the creation of these 1D-ladder states that live on a line of pairs of Carbon atoms. Fig. 9 shows 1D wave functions for all GQD's considered in Sec. IV and for graphene clusters with periodic boundary conditions. It is clear that the number of 1D wave functions depends strongly on the boundary conditions. Therefore hexagonal GQD's with armchair edges (Fig. 9(d)) favour the presence of these states, which exist for all system sizes (see Table V).

We should note that these 1D wave functions do not necessarily exist on a straight line, as seen in Fig. 9(b), (c) and (e). In these cases, boundaries allow a bended 1D string of site pairs within the dot allowing for the rather complicated scaling functions of these states in Table V. Such 1D wave functions also exist in graphene

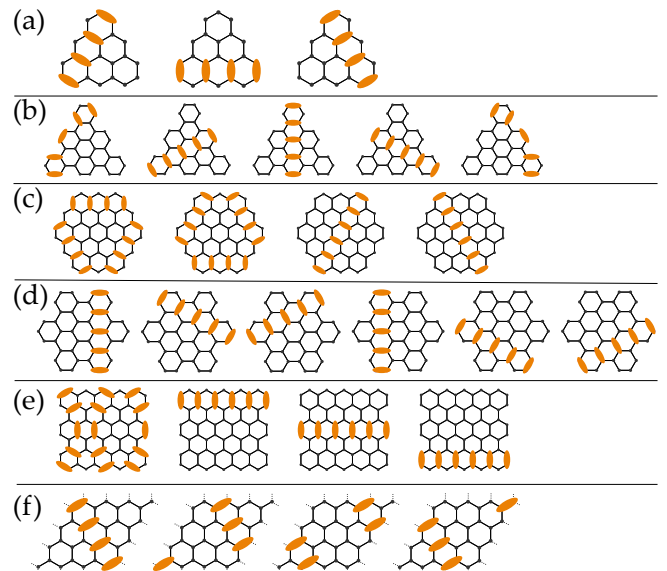


FIG. 9. Examples for 1-dimensional wave functions in graphene quantum dots (GQDs) and bulk graphene. (a) Triangular zigzag, (b) triangular armchair, (c) hexagonal zigzag, (d) hexagonal armchair, (e) rectangular and (f) cluster with periodic boundary conditions (graphene). Boundary conditions set the number and shape of allowed 1-dimensional states (see scaling behaviour in Tab. V), which do not necessarily have to proceed in a straight line, as seen in the first example of (e).

clusters with periodic boundary conditions, as shown in Fig. 9(f).

The one-dimensional character of states at  $\epsilon = \pm t$  provides a plausible explanation for the large exciton binding energies of  $\sim 500$  meV found in graphene<sup>37–41</sup>, since confinement in one-dimension greatly enhances binding. Furthermore, optical resonances in carbon nanotubes are predicted to arise from strongly-correlated 1D excitons<sup>81</sup>. Their binding energies have been predicted with  $\sim 400$  meV<sup>82</sup>, comparably close to the results for graphene.

In summary, we have shown that eigenstates with energy  $\epsilon = \pm t$  show a 1D character and can exist in both GQD's and graphene. Their 1D nature provides a possible explanation for the unusually high exciton binding energies found at the M-point in graphene<sup>37–41</sup>.

## VI. DISORDER IN A GRAPHENE QUANTUM DOT : THE ROLE OF VACANCIES AND ASYMMETRY

Even though GQD's can be produced in predefined regular shapes<sup>30–34</sup>, techniques like chemical vapour deposition (CVD) or temperature programmed growth (TPG) result in dots with irregular shapes<sup>29</sup>. Furthermore, surface contamination with adatoms during the fabrication process can introduce scattering potentials, which change

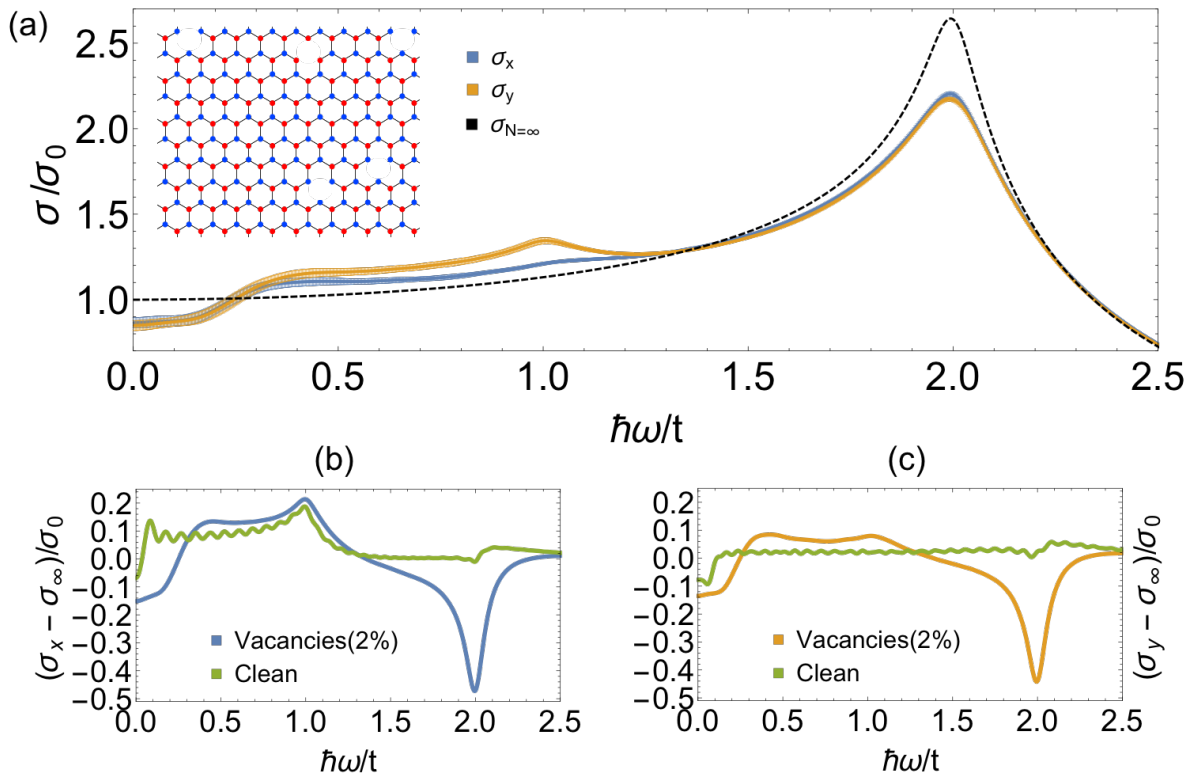


FIG. 10. Effect of random site vacancies on the optical conductivity of a rectangular graphene quantum dot (GQD). (a) Optical conductivity of an ensemble of disordered GQD's, for  $x$ -polarized (blue curve) and  $y$ -polarized (yellow curve) light. Error bars show the standard deviation of results with the ensemble, while the dashed line shows equivalent results for an infinite graphene sheet, without vacancies. (b) Difference between optical conductivity of clean and disordered GQD's and an infinite graphene sheet, for  $x$ -polarized light. (c) Equivalent results for  $y$ -polarized light. The disordered GQD shows additional features in the visible spectrum, while the dominant absorption peak at  $\hbar\omega/t = 2$  is reduced. Results were calculated from Eq. (16), within a tight-binding model for a GQD with  $N \approx 10,000$  sites, setting  $\gamma/t = 0.05$ . Disorder-averages were calculated for 2% of randomly introduced vacancies, and averaged over  $\approx 100$  realisations.

the electronic properties of the GQD's. In the previous sections, we explained how the geometry of GQD's impacts their optical properties and showed that the presence of zigzag edges results in an additional peak in the optical conductivity at low frequencies. It is therefore useful to examine to which extent these features can survive in the case of irregular shaped dots.

Here we discuss two of such cases: (a) rectangular GQD's with single atom vacancies, and (b) GQD's with asymmetric shape.

#### A. The role of vacancies

The role of vacancies on the electronic properties of graphene and its nanostructures has been extensively studied<sup>83,84</sup>. Moreover, it has been shown that metallic adatoms on the graphene's surface – a common source of contamination during fabrication – can be treated theoretically as an atomic vacancy on the graphene lattice in

the case of strong local scattering potentials.<sup>85</sup>

Here, we discuss the effect of vacancies on the optical conductivity of rectangular GQD's. As explained in Sec. IV, for clean, vacancy-free dots, optical excitation polarized along the zigzag edges captures signatures of zero-energy, edge modes in the form of a peak at  $\hbar\omega = t$ . This peak is absent for polarization along the armchair edges, allowing a distinction between different edge types. We now calculate the optical conductivity for dots with a number of randomly introduced vacancies on the lattice. In our model, we set electron hopping to/from the vacancy sites to zero, which is equivalent to an infinite on-site energy at the vacancies.

Fig. 10(a) shows the optical conductivities  $\sigma_x(\omega)$  and  $\sigma_y(\omega)$  for rectangular GQD's of size  $N \approx 10,000$  and 2% vacancies. In comparison with the graphene limit,  $\sigma_{N=\infty}(\omega)$  (Eq. 18), both polarization directions show an enhanced shoulder in the visible region of the spectrum,  $\hbar\omega/t \approx 1$  and a decrease of intensity at  $\hbar\omega/t = 2$ .

This is more clearly seen in Fig. 10(b) and (c) where



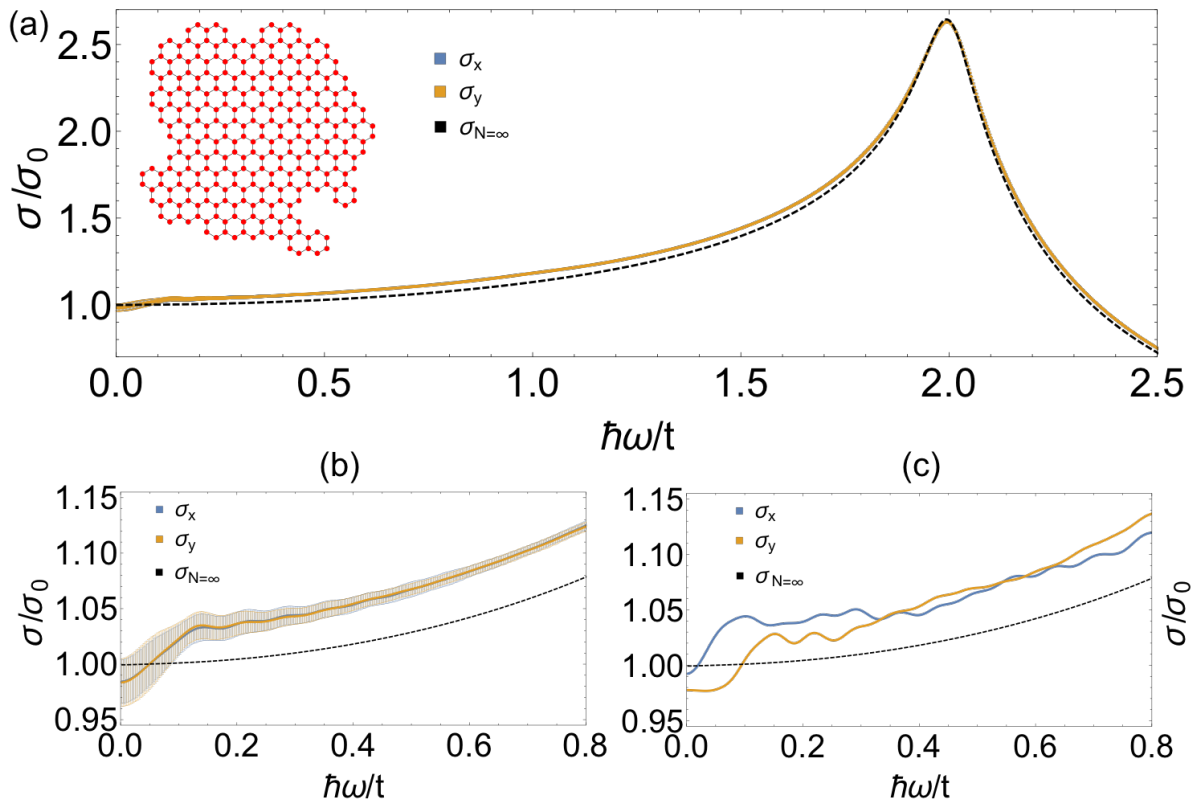


FIG. 11. Effect of edge-disorder on the optical conductivity of a graphene quantum dot (GQD). (a) Optical conductivity of an ensemble of disordered GQD's, for  $x$ -polarized (blue curve) and  $y$ -polarized (yellow curve) light. The dashed line shows equivalent results for an infinite graphene sheet, without disorder. (b) Detail of the optical conductivity of disordered GQD's at low frequencies. Error bars show the standard deviation within the ensemble. (c) Optical conductivity of an individual disordered GQD at low frequencies, showing the difference between  $x$ - and  $y$ -polarized light. Results were calculated from Eq. (16), within a tight-binding model for a GQD with  $N \approx 10,800$  sites, setting  $\gamma/t = 0.05$ . Disorder-averages were calculated for an ensemble of  $\approx 100$  realisations.

the difference  $\sigma(\omega) - \sigma_{N=\infty}(\omega)$  for both clean GQD's and dots with 2% vacancies is plotted. The dominant peak at  $\hbar\omega/t = 2$  is significantly reduced by the presence of vacancies. Similarly, for  $\hbar\omega/t \approx 1$ , the vacancies result in an enhanced shoulder for  $\sigma_y$ , which is absent in the clean GQD. For  $\sigma_x$ , this shoulder is only slightly larger than the one already present for vacancy-free dots.

These features can be explained by the fact that every single vacancy on the graphene lattice creates a zigzag edge around it, which can be seen as an inverse zigzag triangular dot. Therefore additional zero-energy states can be formed along these edges, which allow scattering to the highly degenerate states in the vicinity of the van-Hove singularity and result in the enhanced shoulder in the visible region of the spectrum.

On the other hand, the presence of vacancies destroys some of 1D-wave functions with energy  $\epsilon = \pm t$  (see Sec. V). Consequently, the dominant absorption peak at  $\hbar\omega = 2t$ , which is created by transition between such states, is reduced.

Our findings are consistent with previous results show-

ing that vacancies in graphene result in the formation of localised states<sup>83</sup>. Also, calculations in disordered graphene show it exhibits midgap states in the density of states<sup>86,87</sup> and an additional peak in the optical conductivity<sup>9</sup>.

## B. The role of asymmetry

Asymmetry is an unavoidable issue in the fabrication of GQD's. Techniques like chemical vapour deposition (CVD) and temperature programmed growth (TPG) result in GQDs with a variety of shapes and sizes, even with holes<sup>29</sup>. Even techniques that can create GQD's with a predefined shape are not free of errors<sup>30-34</sup>.

Here we address this case, by calculating the optical conductivity  $\sigma(\omega)$  for asymmetric dots, showing a random mixture of armchair and zigzag edges.

Fig. 11(a) shows the optical conductivity  $\sigma(\omega)$  for  $x$ - and  $y$ -polarized light for asymmetric GQD's of size  $N \approx 10,800$ , averaged over  $\approx 100$  dots. The mean value of the

optical conductivity is very close to the infinite graphene limit, since edge-effects are averaged out. The small offset from the graphene limit is due to finite-size effects.

The effect of averaging is shown more clearly in Figs. 11(b) and (c). Even though on average,  $\sigma_x$  and  $\sigma_y$  coincide (Fig. 11(b)), for each individual dot they do not (Fig. 11(c)), due to an absence of symmetry.

## VII. CONCLUSIONS

The discovery of Graphene, more than 10 years ago<sup>1,2</sup>, has sparked a renaissance in the study of two-dimensional materials, and their potential technological applications<sup>88,89</sup>. Graphene quantum dots (GQD's), offer yet another new opportunity, to control the properties of a graphene sheet by restricting its size and shape<sup>18,19</sup>. In particular, the ability to control the optical properties of GQD's has potential applications in fields ranging from quantum computation to solar energy<sup>20-28</sup>. However, tailoring the properties of a GQD to a specific application requires the ability to fabricate dots with the desired shape, or to post-select for dots with a given shape after fabrication. In either case, understanding the relationship between the size and shape of the dot and its physical properties is paramount.

In this Article, we have explored the role that size, shape, edge-type and atomic vacancies play in the optical conductivity of GQD's. Using group theory, we determined the optical selection rules which follow from the symmetry of a regular-shaped GQD. We find that the optical response is *independent* of the polarization of the incident light in triangular or hexagonal GQD's, which have an abelian point-group symmetry [cf. Fig. 2, Fig. 3]. Meanwhile the optical conductivity is *polarization-dependent* in rectangular GQD's, which have a non-abelian point-group symmetry [cf. Fig. 4].

We have also explored the optical conductivity  $\sigma(\omega)$  of GQD's within a simple tight-binding model [Eq. (3)], known to give a good account of the properties of bulk graphene [45]. For small GQD's,  $\sigma(\omega)$  depends strongly on the type of dot considered, and has many non-universal features [cf. Fig. 5]. These features evolve with size, and the optical response of GQD's of intermediate size ( $N \gtrsim 5,000$  sites,  $L \gtrsim 10\text{nm}$ ) has much in common with the response of bulk graphene. In particular this shows a strong peak for UV light, as observed, in the bulk. None the less, for dots of this size,  $\sigma(\omega)$  still retains tell-tale features which provide important information about edge-geometry of the dot. In particular, we find an additional peak in the optical conductivity at the UV end of the visible spectrum in GQD's with zigzag edges [cf. Fig. 6].

Within a tight-binding model, both of these peaks in the optical conductivity are intimately connected with the existence of states with energy  $\epsilon = \pm t$ . We have explored the nature of the wave functions of these states in different-shaped GQD's, and find that they have

a one-dimensional character [cf. Fig. 8]. Equivalent one-dimensional states also exist for clusters with periodic boundary conditions, where they occur at the M-point in the Brillouin zone (i.e.  $\mathbf{k}_1 = (\frac{2\pi}{3\sqrt{3}}, \frac{2\pi}{3})$  and  $\mathbf{k}_2 = (\frac{4\pi}{3\sqrt{3}}, 0)$ ), and are associated with Van Hove singularities in the single-particle density of states. The one-dimensionality of these wave functions provide a very natural explanation for large binding energies of excitons formed of particles and holes near the M-point<sup>37-41</sup>.

Finally, we discussed the effect of shape-asymmetry and atomic vacancies in the optical response of GQD's. We showed that atomic vacancies in the lattice enhance the peak in the optical conductivity arising from zigzag edges [cf. Fig. 10]. This is a signature of additional localization around the vacancy sites. In the case of completely asymmetric GQD's, the optical conductivity is polarization-dependent, although those effects may not be measurable for large distributions of randomly shaped dots [cf. Fig. 11].

An important open question for future studies of the optical properties of GQD's is the effect of electron-electron interactions. Since the optical selection rules derived in this Article are fully determined by the symmetry of the dot alone, these will remain valid. However, interactions can have a profound effect on electrons on the edges of graphene sheets<sup>70,90-92</sup>, and we anticipate that they will also have an effect on the optical response of GQD's.

The effect of interactions will be most pronounced in small dots, where magnetic effects will be important, and many of the individual peaks will be split by interactions. In larger dots, where the optical response is a smooth function of frequency, we anticipate that the effects of interactions will be much more benign, and lead mainly to a renormalisation of energy scales. A prototype for this is provided by the strong peak in the optical response of bulk graphene in the UV spectrum, at  $\hbar\omega = 4.6\text{ eV}$ <sup>39</sup>. Within a simple (non-interacting) tight-binding model [cf. Eq. (3)] this peak reflects transitions between states with energy  $E \sim \pm t$ , and with the usual parameterisation,  $t = 2.8\text{ eV}$  [45], it would be expected to occur for  $\hbar\omega = 5.6\text{ eV}$ . However in bulk graphene the particle-hole pairs associated with this peak can be viewed as excitons, and interactions lead to finite binding-energy, shifting the peak to lower energies<sup>37-41</sup>. The same should be true for the equivalent, "2t" peak in GQD's of intermediate to large size [cf. Fig. 5]. And we anticipate that interactions will also lead to a shift in the peak at  $\hbar\omega \sim t$ , observed for GQD's with zigzag edges and/or vacancies [cf. Fig. 6, Fig. 11]. This expectation remains to be verified, but we hope that the results in this Article will provide a good starting point for future studies.

And for now, the most exciting prospect remains the measurement of the optical response of GQD's in experiment. As GQD's with regular and irregular shapes are currently available [cf. e.g. Ref. 33 and 34], this is a very real possibility.

## ACKNOWLEDGMENTS

This work was supported by the Theory of Quantum Matter Unit and the Femtosecond Spectroscopy Unit of the Okinawa Institute of Science and Technology Graduate University. E.K. was partially supported by the European Union, Seventh Framework Programme (FP7-REGPOT-2012-2013-1) under grant agreement 316165.

## Appendix A: Optical selection rules for hexagonal dots

$D_6$	$E$	$2C_6$	$2C_3$	$C_2$	$3C'_2$	$3C''_2$
$A_1$	1	1	1	1	1	1
$A_2$	1	1	1	1	-1	-1
$B_1$	1	-1	1	-1	1	-1
$B_2$	1	-1	1	-1	-1	1
$E_1$	2	1	-1	-2	0	0
$E_2$	2	-1	-1	2	0	0

TABLE VI. Character Table of the point-group  $D_6$ , describing the symmetry of hexagonal graphene quantum dots (GQD's) of the type shown in Fig. 1(c) and Fig. 1(d). Eigenstates of a hexagonal GQD transform with irreducible representations (irreps)  $A_1$ ,  $A_2$ ,  $B_1$ ,  $B_2$ ,  $E_1$  and  $E_2$ . The corresponding symmetry operations  $E$ ,  $C_6$ ,  $C_3$  and  $C_2$  are defined in Appendix A.

Hexagonal GQD's have to a non-abelian point-group symmetry, analogous to the triangular GQD's that we discussed in detail in Sec. III. Here we show that the optical conductivity is also polarization-independent for these dots. The non-abelian point-group symmetry of hexagonal GQD's is  $D_6$  (Table VI).

Using the same analysis as in the case of triangular GQD's, we obtain optical selection rules shown in Table VII. As expected, the selection rules are again independent of the polarization.

Fig. 12(a) shows the polarization-independent optical conductivity for  $x$ - and  $y$ -polarized light. Optical energy

	x	y
$C'_2$	$A_1, B_1, E_{1,2} \leftrightarrow A_2, B_2, E_{1,2}$	$A_1, B_1, E_{1,2} \leftrightarrow A_1, B_1, E_{1,2}$ $A_2, B_2, E_{1,2} \leftrightarrow A_2, B_2, E_{1,2}$
$C_6$	$A_{1,2} \leftrightarrow E_1; \quad B_{1,2} \leftrightarrow E_2; \quad E_{1,2} \leftrightarrow E_{1,2}$	
total	$A_{1,2} \leftrightarrow E_1$ $B_{1,2} \leftrightarrow E_2$ $E_1 \leftrightarrow E_2$	$A_{1,2} \leftrightarrow E_1$ $B_{1,2} \leftrightarrow E_2$ $E_1 \leftrightarrow E_2$

TABLE VII. Selection rules for optical transitions in hexagonal Graphene Quantum Dots (GQD's) of the type shown in Fig. 1 (c) and (d). While individual transitions may be sensitive to polarization, the total response does not distinguish between  $x$ - and  $y$ -polarized light.

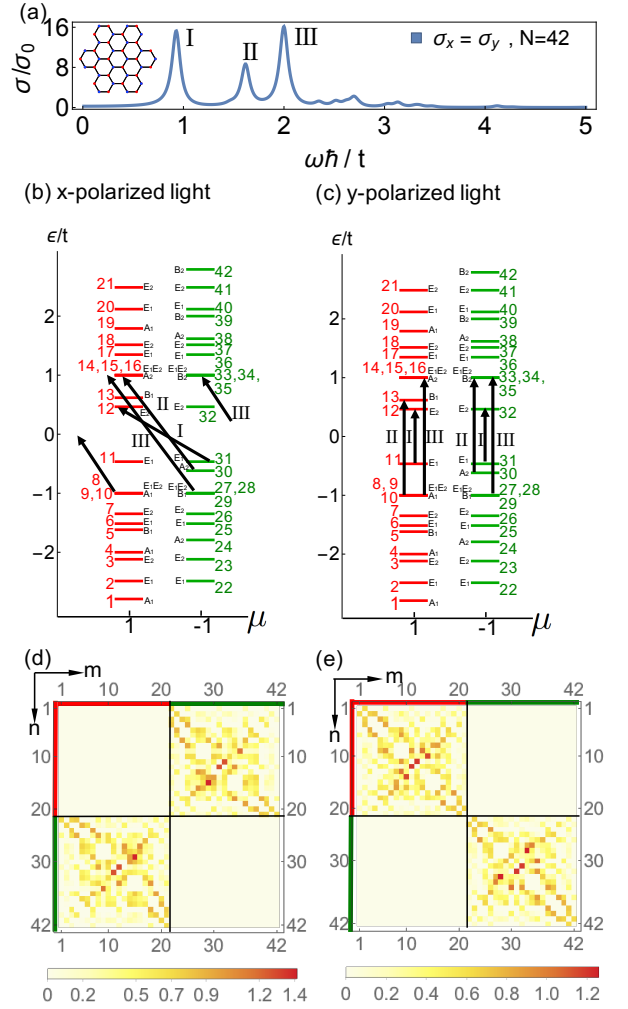


FIG. 12. Optical selection rules for a hexagonal graphene quantum dot (GQD), in linearly-polarized light. (a) Optical conductivity  $\sigma(\omega)$ , showing equivalence of results for  $x$ - and  $y$ - polarized light. (b) and (c) Spectrum of the corresponding tight-binding model Eq. (3), in the mirror basis Eq. (20), showing the different allowed transitions for  $x$ - and  $y$ -polarized light. (d) and (e) Matrix elements of the corresponding current operators  $|j_{nm,x}|^2$  and  $|j_{nm,y}|^2$  [cf. Eq. (14)]. Results for  $\sigma(\omega)$  were calculated from Eq. (16), setting  $\gamma/t = 0.05$ , for the smallest hexagonal GQD with armchair edges ( $N = 42$ ). Eigenstates are labelled according to their quantum number  $n = 1 \dots 42$ , eigenvalue  $\mu = \pm 1$  [Eq. (20)] and corresponding irrep [cf. Table VI].

transitions between symmetric and anti-symmetric states under reflection at the  $y$ -axis are shown in Fig. 12(b) and (c) respectively. Black arrows show energy transitions dominantly contributing to the optical conductivity in (a). The matrix elements of the current operator in the  $x$ - and  $y$ -direction are shown in Fig. 12(d) and (e) respectively.

Similarly, Fig. 13(a) shows the optical conductivity for left- and right circularly polarized light. It is identical with Fig. 12(a). Optical energy transitions between

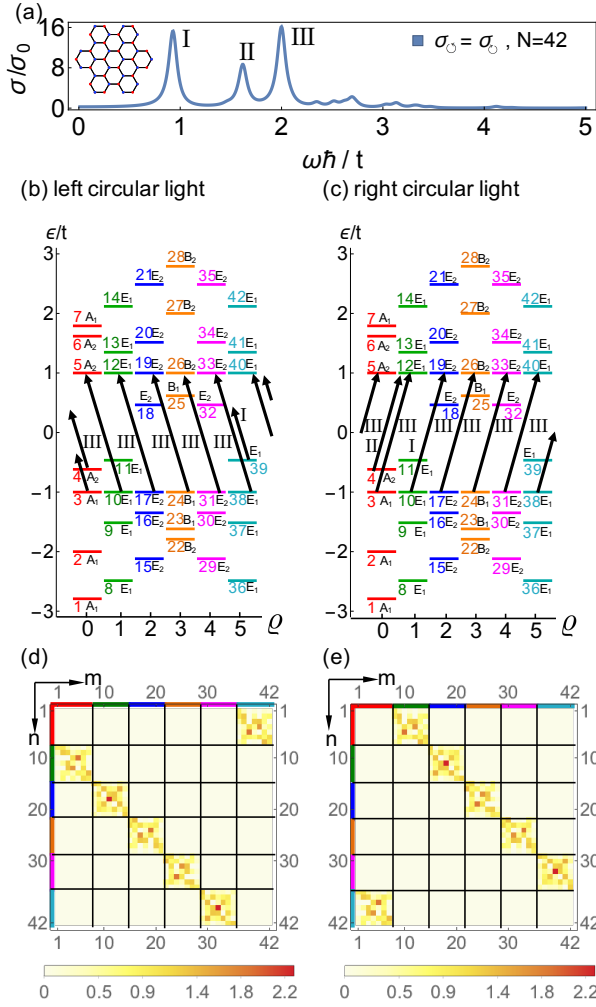


FIG. 13. Optical selection rules for a hexagonal graphene quantum dot (GQD), in circularly-polarized light. (a) Optical conductivity  $\sigma(\omega)$ , showing equivalence of results for left- and right- circularly polarized light. (b) and (c) Spectrum of the corresponding tight-binding model Eq. (3), in the rotation basis Eq. (28), showing the different allowed transitions for left- and right- circularly polarized light. (d) and (e) Matrix elements of the corresponding current operators  $|j_{nm,\odot}|^2$  and  $|j_{nm,\ominus}|^2$  [cf. Eq. (14)]. Results for  $\sigma(\omega)$  were calculated from Eq. (16), setting  $\gamma/t = 0.05$ , for the smallest hexagonal GQD with armchair edges ( $N = 42$ ). Eigenstates are labelled according to their quantum number  $n = 1 \dots 42$ , eigenvalue  $\mu_n = e^{i\frac{2\pi}{3}\rho_n}$ ,  $\rho_n = 0, 1, 2$  [Eq. (29)] and corresponding irrep [cf. Table VI].

states of different Irreps are shown in Fig. 13(b) and (c) respectively. Black arrows show energy transitions dominantly contributing to the optical conductivity in (a). The matrix elements of the current operator for left- and right-circularly polarized light are shown in Fig. 13(d) and (e) respectively.

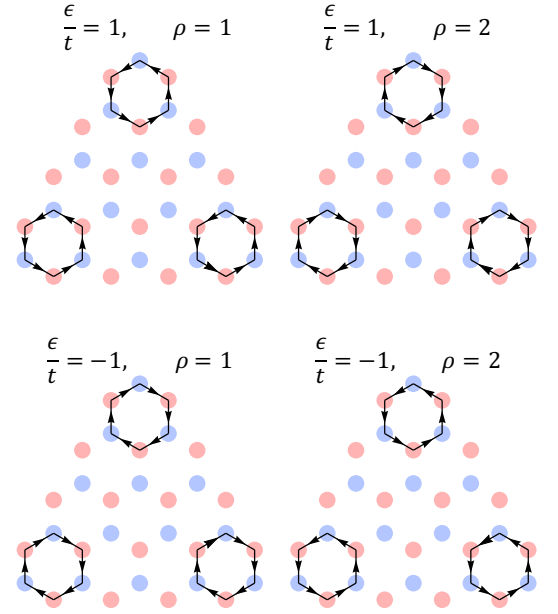


FIG. 14. Distribution of the current on bonds within the Kramers-doublet states in triangular graphene quantum dots (GQD's). By choosing a vector basis of the Hamiltonian Eq. (3), which respects the rotational symmetry of the dot (see Eq. (28)), we can distinguish between states with  $\rho = 1, 2$ , showing a net circulation of current on their bonds. Hereby, states at  $\hbar\omega/t = \pm 1$  show non-zero currents at the edges of the GQD. Results are shown for a GQD with zigzag edges of size  $N = 33$ .

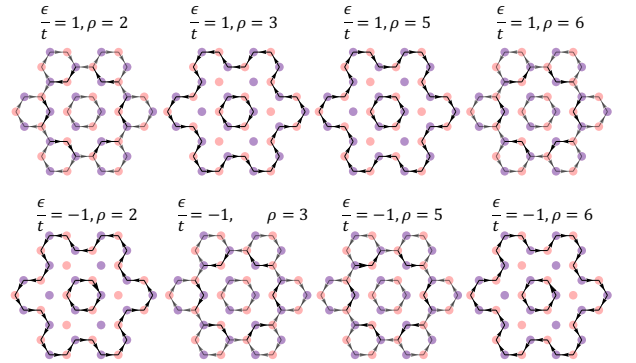


FIG. 15. Distribution of the current on bonds within the Kramers-doublet states in hexagonal graphene quantum dots (GQD's). By choosing a vector basis of the Hamiltonian Eq. (3), which respects the rotational symmetry of the dot (see Eq. (28)), we can distinguish between states with  $\rho = 1, 2, 4, 5$  (see Fig. 13), showing a net circulation of current on their bonds. Results are shown for a GQD with armchair edges of size  $N = 42$ .

## Appendix B: Kramers doublets in triangular graphene quantum dots

We recognised in Sec. III A 2 the existence of doubly degenerate states of Irrep  $E$ , forming Kramers doublets

with time-reversal symmetry. The representation of the Hamiltonian in the basis of the rotational operator gives us access to these states.

In Fig. 14 and Fig. 15 we plot the current (black arrows) within a triangular ( $N = 33$ ) and hexagonal ( $N = 42$ ) GQD for energies  $\epsilon = \pm t$  for the Kramers doublets. The direction of the current within the dot is oriented in the opposite direction, which ensures the time reversal symmetry. An external magnetic field would break this time reversal symmetry and lift the degeneracy of the Kramers Doublets. We would then see changes in the optical absorption spectrum, which can lead to possible manipulations of magnetic moments in GQD's<sup>78</sup>.

In Fig. 14 we find currents localised on the tips of the triangle, while in Fig. 15 currents proceed in a circular fashion within the whole dot. We find an absence of currents for states with  $\epsilon = 0$ .

### Appendix C: Estimate of exciton binding energy within one-dimensional wave functions

Calculations of  $\sigma(\omega)$  within a tight-binding model [Eq. (3)] of an extended graphene sheet show a pronounced peak for  $\hbar\omega \sim 2t$  [8 and 10]. The same is true of a sufficiently large GQD [cf. Fig. 5]. In experiments on graphene sheets this peak is not observed at  $\hbar\omega = 2t \approx 5.6\text{eV}$ , but at the lower energy of  $\hbar\omega = 4.6\text{eV}$  (see e.g. Ref. 39) — a red-shift of  $\sim 1\text{eV}$ . This shift is usually ascribed to the binding-energy of an exciton formed of particle-hole pairs, due to the interaction be-

tween electrons<sup>37,57,93–96</sup>.

Building on the insight that electronic states at energy  $\epsilon = \pm t$  have one-dimensional character [cf. Fig. 9, Section V], and are built of two electrons confined to two sites [cf. Fig. 8], we can make a very simple estimate of the exciton binding by considering the two-site Hubbard model

$$\hat{\mathcal{H}} = -t(\hat{c}_{1,\uparrow}^\dagger \hat{c}_{2,\uparrow} + \hat{c}_{2,\uparrow}^\dagger \hat{c}_{1,\uparrow} + \hat{c}_{1,\downarrow}^\dagger \hat{c}_{2,\downarrow} + \hat{c}_{2,\downarrow}^\dagger \hat{c}_{1,\downarrow}) + U(\hat{n}_{1,\uparrow}\hat{n}_{1,\downarrow} + \hat{n}_{2,\uparrow}\hat{n}_{2,\downarrow}). \quad (\text{C1})$$

Diagonalising this Hamiltonian, we find the eigenvalues

$$\epsilon_0 = \frac{1}{2}(U - \sqrt{16t^2 + U^2}) \quad (\text{C2})$$

$$\epsilon_1 = 0 \quad (\text{C3})$$

$$\epsilon_2 = U \quad (\text{C4})$$

$$\epsilon_3 = \frac{1}{2}(U + \sqrt{16t^2 + U^2}). \quad (\text{C5})$$

Optical selection rules allow transitions from the lowest lying energy state with  $\epsilon_0$  to the intermediate states  $\epsilon_1, \epsilon_2$ . Since the interaction potential  $U$  will lift their degeneracy, low-energy transitions will just occur between  $\epsilon_0$  and  $\epsilon_1$ , where we find that

$$\Delta\epsilon = \epsilon_1 - \epsilon_0 = 4.6\text{eV} \quad (\text{C6})$$

for  $U \approx 2.2\text{eV}$ . This compares with estimates of on-site potential  $U \sim 9.3 - 10.1\text{eV}$  in the published literature<sup>97,98</sup>.

- 
- <sup>1</sup> K. S. Novoselov, *Science* **306**, 666 (2004).
  - <sup>2</sup> K. S. Novoselov, A. K. Geim, S. V. Morozov, D. Jiang, M. I. Katsnelson, I. V. Grigorieva, S. V. Dubonos, and A. A. Firsov, *Nature* **438**, 197 (2005).
  - <sup>3</sup> R. R. Nair, P. Blake, A. N. Grigorenko, K. S. Novoselov, T. J. Booth, T. Stauber, N. M. R. Peres, and A. K. Geim, *Science* **320**, 1308 (2008).
  - <sup>4</sup> T. Ando, Y. Zheng, and H. Suzuura, *Journal of the Physical Society of Japan* **71**, 1318 (2002).
  - <sup>5</sup> V. P. GUSYNIN, S. G. SHARAPOV, and J. P. CARBOTTE, *International Journal of Modern Physics B* **21**, 4611 (2007).
  - <sup>6</sup> K. Ziegler, *Phys. Rev. B* **75**, 233407 (2007).
  - <sup>7</sup> H. Min and A. H. MacDonald, *Phys Rev Lett* **103**, 067402 (2009).
  - <sup>8</sup> T. Stauber, N. M. R. Peres, and A. K. Geim, *Phys. Rev. B* **78**, 085432 (2008).
  - <sup>9</sup> S. Yuan, R. Roldán, H. De Raedt, and M. I. Katsnelson, *Phys. Rev. B* **84**, 195418 (2011).
  - <sup>10</sup> P. V. Buividovich and M. I. Polikarpov, *Phys. Rev. B* **86**, 245117 (2012).
  - <sup>11</sup> A. K. Geim and K. S. Novoselov, *Nat Mater* **6**, 183 (2007).
  - <sup>12</sup> F. Miao, S. Wijeratne, Y. Zhang, U. C. Coskun, W. Bao, and C. N. Lau, *Science* **317**, 1527 (2007).
  - <sup>13</sup> M. I. Katsnelson, *The European Physical Journal B* **51**, 157 (2006).
  - <sup>14</sup> J. Tworzydło, B. Trauzettel, M. Titov, A. Rycerz, and C. W. J. Beenakker, *Phys. Rev. Lett.* **96**, 246802 (2006).
  - <sup>15</sup> S. Ryu, C. Mudry, A. Furusaki, and A. W. W. Ludwig, *Phys. Rev. B* **75**, 205344 (2007).
  - <sup>16</sup> S. Das Sarma, S. Adam, E. H. Hwang, and E. Rossi, *Reviews of Modern Physics* **83**, 407 (2011).
  - <sup>17</sup> V. N. Kotov, B. Uchoa, V. M. Pereira, F. Guinea, and A. H. Castro Neto, *Reviews of Modern Physics* **84**, 1067 (2012).
  - <sup>18</sup> A. M. Silva, M. S. Pires, V. N. Freire, E. L. Albuquerque, D. L. Azevedo, and E. W. S. Caetano, *The Journal of Physical Chemistry C* **114**, 17472 (2010).
  - <sup>19</sup> A. D. Güçlü, P. Potasz, M. Korkusinski, and P. Hawrylak, *Graphene Quantum Dots* (Springer Berlin Heidelberg, 2014).
  - <sup>20</sup> S. Zhu, J. Zhang, C. Qiao, S. Tang, Y. Li, W. Yuan, B. Li, L. Tian, F. Liu, R. Hu, H. Gao, H. Wei, H. Zhang, H. Sun, and B. Yang, *Chemical Communications* **47**, 6858 (2011).
  - <sup>21</sup> S. H. Jin, D. H. Kim, G. H. Jun, S. H. Hong, and S. Jeon, *ACS Nano* **7**, 1239 (2013).
  - <sup>22</sup> P. Roy, A. P. Periasamy, C.-Y. Lin, G.-M. Her, W.-J. Chiu, C.-L. Li, C.-L. Shu, C.-C. Huang, C.-T. Liang, and H.-T. Chang, *Nanoscale* **7**, 2504 (2015).
  - <sup>23</sup> S. Umrao, M.-H. Jang, J.-H. Oh, G. Kim, S. Sahoo, Y.-H.



- Cho, A. Srivastva, and I.-K. Oh, *Carbon* **81**, 514 (2015).
- <sup>24</sup> C. M. Luk, L. B. Tang, W. F. Zhang, S. F. Yu, K. S. Teng, and S. P. Lau, *Journal of Materials Chemistry* **22**, 22378 (2012).
  - <sup>25</sup> D. I. Son, B. W. Kwon, D. H. Park, W.-S. Seo, Y. Yi, B. Angadi, C.-L. Lee, and W. K. Choi, *Nature Nanotechnology* **7**, 465 (2012).
  - <sup>26</sup> G. Konstantatos, M. Badioli, L. Gaudreau, J. Osmond, M. Bernechea, F. P. G. de Arquer, F. Gatti, and F. H. L. Koppens, *Nat Nano* **7**, 363 (2012).
  - <sup>27</sup> Q. Zhang, J. Jie, S. Diao, Z. Shao, Q. Zhang, L. Wang, W. Deng, W. Hu, H. Xia, X. Yuan, and S.-T. Lee, *ACS Nano* **9**, 1561 (2015).
  - <sup>28</sup> Z. M. W. Jiang Wu, ed., *Quantum Dot Solar Cells*, Vol. 15 (Springer New York, 2014).
  - <sup>29</sup> J. Coraux, A. T. N'Diaye, M. Engler, C. Busse, D. Wall, N. Buckanie, F.-J. M. zu Heringdorf, R. van Gastel, B. Poelsema, and T. Michely, *New Journal of Physics* **11**, 023006 (2009).
  - <sup>30</sup> J. Lu, P. S. E. Yeo, C. K. Gan, P. Wu, and K. P. Loh, *Nat Nano*, 247 (2011).
  - <sup>31</sup> X. Li, C. W. Magnuson, A. Venugopal, R. M. Tromp, J. B. Hannon, E. M. Vogel, L. Colombo, and R. S. Ruoff, *Journal of the American Chemical Society* **133**, 2816 (2011).
  - <sup>32</sup> N. Mohanty, D. Moore, Z. Xu, T. S. Sreeprasad, A. Nagaraja, A. A. Rodriguez, and V. Berry, *Nature Communications* **3**, 844 (2012).
  - <sup>33</sup> M. Olle, G. Ceballos, D. Serrate, and P. Gambardella, *Nano Letters* **12**, 4431 (2012).
  - <sup>34</sup> Z. Yan, J. Lin, Z. Peng, Z. Sun, Y. Zhu, L. Li, C. Xiang, E. L. Samuel, C. Kittrell, and J. M. Tour, *ACS Nano* **6**, 9110 (2012).
  - <sup>35</sup> K. Müllen, *ACS Nano* **8**, 6531 (2014).
  - <sup>36</sup> L. Wang, Y. Wang, T. Xu, H. Liao, C. Yao, Y. Liu, Z. Li, Z. Chen, D. Pan, L. Sun, and M. Wu, *Nature Communications* **5**, 1 (2014).
  - <sup>37</sup> L. Yang, J. Deslippe, C.-H. Park, M. L. Cohen, and S. G. Louie, *Phys. Rev. Lett.* **103**, 186802 (2009).
  - <sup>38</sup> V. G. Kravets, A. N. Grigorenko, R. R. Nair, P. Blake, S. Anissimova, K. S. Novoselov, and A. K. Geim, *Phys. Rev. B* **81**, 155413 (2010).
  - <sup>39</sup> K. F. Mak, J. Shan, and T. F. Heinz, *Phys Rev Lett* **106**, 046401 (2011).
  - <sup>40</sup> D.-H. Chae, T. Utikal, S. Weisenburger, H. Giessen, K. v. Klitzing, M. Lippitz, and J. Smet, *Nano Letters* **11**, 1379 (2011).
  - <sup>41</sup> A. Matković, A. Beltaos, M. Milićević, U. Ralević, B. Vasić, D. Jovanović, and R. Gajić, *Journal of Applied Physics* **112**, 123523 (2012).
  - <sup>42</sup> P. R. Wallace, *Phys. Rev.* **71**, 622 (1947).
  - <sup>43</sup> E. Fradkin, *Phys. Rev. B* **33**, 3257 (1986).
  - <sup>44</sup> P. A. Lee, *Phys. Rev. Lett.* **71**, 1887 (1993).
  - <sup>45</sup> A. H. Castro Neto, F. Guinea, N. M. R. Peres, K. S. Novoselov, and A. K. Geim, *Reviews of Modern Physics* **81**, 109 (2009).
  - <sup>46</sup> N. M. R. Peres, *Reviews of Modern Physics* **82**, 2673 (2010).
  - <sup>47</sup> M. I. Katsnelson, *The European Physical Journal B* **51**, 157 (2006).
  - <sup>48</sup> Y. Zhang, Y.-W. Tan, H. L. Stormer, and P. Kim, *Nature* **438**, 201 (2005).
  - <sup>49</sup> V. P. Gusynin and S. G. Sharapov, *Phys. Rev. Lett.* **95**, 146801 (2005).
  - <sup>50</sup> N. Shon and T. Ando, *Journal of the Physical Society of Japan* **67**, 2421 (1998).
  - <sup>51</sup> M. Noro, M. Koshino, and T. Ando, *Journal of the Physical Society of Japan* **79**, 094713 (2010).
  - <sup>52</sup> K. F. Mak, M. Y. Sfeir, Y. Wu, C. H. Lui, J. A. Misewich, and T. F. Heinz, *Phys. Rev. Lett.* **101**, 196405 (2008).
  - <sup>53</sup> A. B. Kuzmenko, E. van Heumen, F. Carbone, and D. van der Marel, *Phys Rev Lett* **100**, 117401 (2008).
  - <sup>54</sup> P. K. Gogoi, I. Santoso, S. Saha, S. Wang, A. H. Castro Neto, K. P. Loh, T. Venkatesan, and A. Rusydi, *EPL (Europhysics Letters)* **99**, 67009 (2012).
  - <sup>55</sup> T. Eberlein, U. Bangert, R. R. Nair, R. Jones, M. Gass, A. L. Bleloch, K. S. Novoselov, A. Geim, and P. R. Bridgdon, *Phys. Rev. B* **77**, 233406 (2008).
  - <sup>56</sup> C. Lee, J. Y. Kim, S. Bae, K. S. Kim, B. H. Hong, and E. J. Choi, *Applied Physics Letters* **98**, 071905 (2011).
  - <sup>57</sup> S. Yuan, R. Roldán, and M. I. Katsnelson, *Phys. Rev. B* **84**, 035439 (2011).
  - <sup>58</sup> T. Yamamoto, T. Noguchi, and K. Watanabe, *Phys. Rev. B* **74**, 121409 (2006).
  - <sup>59</sup> B. Trauzettel, D. V. Bulaev, D. Loss, and G. Burkard, *Nat Phys* **3**, 192 (2007).
  - <sup>60</sup> K. A. Ritter and J. W. Lyding, *Nature Materials* **8**, 235 (2009).
  - <sup>61</sup> S. K. Hämäläinen, Z. Sun, M. P. Boneschanscher, A. Upst, M. Ijäs, A. Harju, D. Vanmaekelbergh, and P. Liljeroth, *Phys. Rev. Lett.* **107**, 236803 (2011).
  - <sup>62</sup> D. Subramaniam, F. Libisch, Y. Li, C. Pauly, V. Geringer, R. Reiter, T. Mashoff, M. Liebmann, J. Burgdörfer, C. Busse, T. Michely, R. Mazzarello, M. Pratzner, and M. Morgenstern, *Phys. Rev. Lett.* **108**, 046801 (2012).
  - <sup>63</sup> W. Jolie, F. Craes, M. Petrović, N. Atodiresi, V. Caciuc, S. Blügel, M. Kralj, T. Michely, and C. Busse, *Phys. Rev. B* **89**, 155435 (2014).
  - <sup>64</sup> M. Zarenia, A. Chaves, G. A. Farias, and F. M. Peeters, *Phys. Rev. B* **84**, 245403 (2011).
  - <sup>65</sup> M. Ezawa, *Phys. Rev. B* **76**, 245415 (2007).
  - <sup>66</sup> P. Potasz, A. D. Güçlü, and P. Hawrylak, *Phys. Rev. B* **81**, 033403 (2010).
  - <sup>67</sup> Z. Z. Zhang, K. Chang, and F. M. Peeters, *Phys. Rev. B* **77**, 235411 (2008).
  - <sup>68</sup> A. D. Güçlü, P. Potasz, O. Voznyy, M. Korkusinski, and P. Hawrylak, *Phys. Rev. Lett.* **103**, 246805 (2009).
  - <sup>69</sup> P. Potasz, A. D. Güçlü, A. Wójs, and P. Hawrylak, *Phys. Rev. B* **85**, 075431 (2012).
  - <sup>70</sup> A. D. Güçlü and P. Hawrylak, *Phys. Rev. B* **87**, 035425 (2013).
  - <sup>71</sup> L. Yang, M. L. Cohen, and S. G. Louie, *Nano Letters* **7**, 3112 (2007).
  - <sup>72</sup> I. Ozfidan, M. Korkusinski, A. D. Güçlü, J. A. McGuire, and P. Hawrylak, *Phys. Rev. B* **89**, 085310 (2014).
  - <sup>73</sup> J. Akola, H. P. Heiskanen, and M. Manninen, *Physical Review B* **77**, 193410 (2008).
  - <sup>74</sup> G. D. Mahan, *Many-Particle Physics*, Vol. 15 (Springer US, 2000).
  - <sup>75</sup> D. Cabib and T. A. Kaplan, *physica status solidi (b)* **58**, 85 (1973).
  - <sup>76</sup> A. L. KUZEMSKY, *International Journal of Modern Physics B* **25**, 3071 (2011).
  - <sup>77</sup> Conservation of angular momentum follows from a continuous rotation symmetry, through Noether's theorem.
  - <sup>78</sup> E. G. Kavousanaki and K. M. Dani, *Phys. Rev. B* **91**, 035433 (2015).
  - <sup>79</sup> A. Zhou and W. Sheng, *Journal of Applied Physics* **112**, 094313 (2012).

- <sup>80</sup> U. Fano, *Phys. Rev.* **124**, 1866 (1961).
- <sup>81</sup> T. Ando, *Journal of the Physical Society of Japan* **66**, 1066 (1997).
- <sup>82</sup> F. Wang, *Science* **308**, 838 (2005).
- <sup>83</sup> V. M. Pereira, F. Guinea, J. M. B. Lopes dos Santos, N. M. R. Peres, and A. H. Castro Neto, *Phys. Rev. Lett.* **96**, 036801 (2006).
- <sup>84</sup> N. M. R. Peres, F. Guinea, and A. H. Castro Neto, *Phys. Rev. B* **73**, 125411 (2006).
- <sup>85</sup> S. Yuan, H. De Raedt, and M. I. Katsnelson, *Phys. Rev. B* **82**, 115448 (2010).
- <sup>86</sup> M. M. Ugeda, D. Fernández-Torre, I. Brihuega, P. Pou, A. J. Martínez-Galera, R. Pérez, and J. M. Gómez-Rodríguez, *Phys. Rev. Lett.* **107**, 116803 (2011).
- <sup>87</sup> M. M. Ugeda, I. Brihuega, F. Guinea, and J. M. Gómez-Rodríguez, *Phys. Rev. Lett.* **104**, 096804 (2010).
- <sup>88</sup> P. Avouris and C. Dimitrakopoulos, *Materials Today* **15**, 86 (2012).
- <sup>89</sup> X. Luo, T. Qiu, W. Lu, and Z. Ni, *Materials Science and Engineering: R: Reports* **74**, 351 (2013).
- <sup>90</sup> M. Fujita, K. Wakabayashi, K. Nakada, and K. Kusakabe, *Journal of the Physical Society of Japan* **65**, 1920 (1996).
- <sup>91</sup> H. Feldner, Z. Y. Meng, A. Honecker, D. Cabra, S. Wessel, and F. F. Assaad, *Phys. Rev. B* **81**, 115416 (2010).
- <sup>92</sup> K. Sasaki and R. Saito, *Journal of the Physical Society of Japan* **77**, 054703 (2008).
- <sup>93</sup> I. F. Herbut, V. Juričić, and O. Vafek, *Phys. Rev. Lett.* **100**, 046403 (2008).
- <sup>94</sup> L. Fritz, J. Schmalian, M. Müller, and S. Sachdev, *Phys. Rev. B* **78**, 085416 (2008).
- <sup>95</sup> L. Yang, *Phys. Rev. B* **83**, 085405 (2011).
- <sup>96</sup> L. Yang, *Nano Letters* **11**, 3844 (2011).
- <sup>97</sup> T. O. Wehling, E. Şaşıoğlu, C. Friedrich, A. I. Lichtenstein, M. I. Katsnelson, and S. Blügel, *Phys. Rev. Lett.* **106**, 236805 (2011).
- <sup>98</sup> M. Schüler, M. Rösner, T. O. Wehling, A. I. Lichtenstein, and M. I. Katsnelson, *Phys. Rev. Lett.* **111**, 036601 (2013).